

Quantifying the Frequency and Orientation of Mitoses in Embryonic Epithelia

by

Parthipan Siva

A thesis
presented to the University of Waterloo
in fulfillment of the
thesis requirement for the degree of
Master of Applied Science
in
Systems Design Engineering

Waterloo, Ontario, Canada, 2007

© Parthipan Siva 2007

I hereby declare that I am the sole author of this thesis. This is a true copy of the thesis, including any required final revisions, as accepted by my examiners.

I understand that my thesis may be made electronically available to the public.

Abstract

The miraculous birth of a new life starts by the formation of an embryo. The process by which an embryo is formed, embryogenesis, has been studied and shown to consist of three types of processes: mitosis, cell differentiation and morphogenetic movements. Scientists and medical doctors are still at a loss to explain the fundamental forces driving embryo development and the causes of birth defects remain largely unknown.

Recent efforts by the Embryo Biomechanics Lab at the University of Waterloo have shown a relationship between morphogenetic movements that occur during embryo formation and the frequency and orientation of mitosis. To further study this relationship a means of automatically identifying the frequency and orientation of mitosis on time-lapse images of embryo epithelia is needed.

Past efforts at identifying mitosis have been limited to the study of cell cultures and stained tissue segments. Two methods for identifying mitosis in contiguous sheets of cells are developed. The first method is based on local motion analysis and the second method is based on intensity analysis.

These algorithms were tested on images of early and late stage embryos of the axolotl (*Ambystoma mexicanum*), a type of amphibian. The performance of the algorithms were measured using the *F-Measure*. The *F-Measure* determines the performance of the algorithm as the true mitosis detection rate penalized by the false mitosis detection rate. The motion based algorithm had performance rates of 68.2% on an early stage image set and 66.7% on a late stage image set, whereas the intensity based algorithm had a performance rates of 73.9% on early stage image set and 90.0% on late stage image set. The mitosis orientation errors for the motion based algorithm were 27.3° average error with a standard deviation (std.) of 19.8° for early stage set and 34.8° average error with a std. of 23.5° for the late stage set. For the intensity based algorithm the orientation errors were 39.8° average with std. of 28.9° for the early stage image set and 15.7° average with std. of 18.9° for the late stage image set.

The intensity based algorithm had the best performance of the two algorithms presented, and the intensity based algorithm performs best on high-magnification images. Its performance is limited by mitoses in adjacent cells and by the presence of natural cell pigment variations.

The algorithms presented here offer a powerful new set of tools for evaluating the role of mitoses in embryo morphogenesis.

Acknowledgements

This work would not be possible without the guidance, support and experience of my supervisors Prof. David A. Clausi and Prof. G. Wayne Brodland. They have given me great latitude to explore the problem at hand, while gently guiding me to its completion. I would also like to thank Caleb Horst who did a wonderful job of getting me the images of the embryos.

Contents

1	Introduction	1
2	Background	5
2.1	Cell Counting	5
2.2	Nucleus Division Identification	7
2.3	Tracking	9
2.3.1	Dynamic Model	10
2.3.2	Measurement Model	11
2.3.3	Kalman Filtering	12
3	Motion Based Algorithm	16
3.1	Mitosis Motion Field Prototype	18
3.2	Image Motion Field	19
3.3	Motion Field Analysis	20
3.3.1	Velocity Orientation Weight	20
3.3.2	Velocity Magnitude Weight	21
3.4	Mitoses Count and Orientation	22
4	Intensity Based Algorithm	24
4.1	Material Reference Frame	26
4.1.1	Key Point Identification and Tracking	29
4.1.2	Triple Junction Point Detection	30
4.2	Intensity Analysis on Material Reference Frame	33
4.3	Mitosis Count and Orientation	36

5	Algorithm Performance	41
5.1	Motion Based Algorithm	43
5.2	Intensity Based Algorithm	46
6	Conclusions and Future Work	56
A	Optical Flow Algorithm	58
B	Triangular Mesh	61
B.1	Derivative Constraint on Mesh Vertices	61
B.2	Barycentric Coordinates	63

List of Tables

5.1	Test Data Sets	42
5.2	Motion Algorithm Parameters	43
5.3	Optimal Threshold Search Range	43
5.4	Intensity Algorithm Parameters	46

List of Figures

1.1	Neurulation	2
1.2	Computer simulation of embryo epithelia	3
1.3	Images of embryo epithelia	3
2.1	Single mitosis	6
2.2	Images of different cell lattices	7
2.3	Cell edges	7
2.4	Cell segmentation result	8
2.5	Comparison of nucleus division in cancer tissue and embryo epithelia	9
2.6	Object representation for tracking	10
2.7	Kalman filtering results for 1D translation	14
2.8	Variance of Kalman filter estimate and measurement	15
3.1	Single mitosis with motion markers	16
3.2	Motion based algorithm overview	17
3.3	Mitosis motion field prototype	18
3.4	Velocity magnitude weighting function	22
4.1	Intensity drop during the division of the nucleus	24
4.2	Intensity based algorithm overview	25
4.3	Obtaining the Material Reference Frame	27
4.4	Triangular mesh deformation	28
4.5	Illustration of aperture problem	29
4.6	Detection of TJPs	31
4.7	Phase Threshold for Lines	32
4.8	TJP masks	32
4.9	Valid and invalid TJPs	33

4.10	Example of the intensity based algorithm	34
4.11	Intensity drop threshold	37
4.12	Nucleus division time	38
4.13	Intensity algorithm orientation	39
5.1	Motion algorithm confusion matrix	44
5.2	PRCs for motion algorithm	45
5.3	Motion algorithm orientation error	46
5.4	Motion algorithm orientation examples	47
5.5	Intensity algorithm confusion matrix	48
5.6	PRC for intensity algorithm	49
5.7	FP due to inaccurate material reference frame.	50
5.8	Multiple mitoses detected as single mitosis.	52
5.9	Intensity algorithm orientation error	53
5.10	Magnification effect on orientation error	54
5.11	Orientation error due to diffused nucleus division	55
B.1	Triangular mesh	62
B.2	Grid connectivity	62
B.3	Mesh and vertex triplets	62
B.4	Deformation of a triangle in the mesh	63

Nomenclature

The following syntax or font style are used for mathematical formulations throughout this text. They are presented here to assist the reader interpret individual formulas used in this text.

Syntax	Definition
\mathbf{A}	Matrix
\underline{a}	Column vector
\vec{a}	Displacement vector or velocity
\hat{a}	Estimate of a
\mathbf{A}	List of vectors ($\mathbf{A}(i) = \underline{a}$).
\mathcal{A}	Vector field; each index is a 2D velocity ($\mathcal{A}(i, j) = \vec{a}$)
$a : i : b$	Matlab notation referring to a set of numbers between a and b inclusive at increments of i

Chapter 1

Introduction

Embryogenesis, the process by which an embryo is formed, can be considered to consist of three main processes: mitosis, cell differentiation and morphogenetic movements. Repeated mitoses, or cell divisions, enable a single-celled zygote (fertilized egg) to give rise to a multi-celled embryo, while cell differentiation enables the cells so produced to become functionally different from each other. Morphogenetic movements then move the differentiated cells to their correct locations and give the embryo its proper form. Organized patterns of cell division can contribute to these movements, and this capacity motivates the present study, the object of which is to identify the locations and orientations of mitoses during early embryo development.

One of the earliest and most important developmental events to occur in vertebrate embryos is neurulation, a process during which a flat sheet of epithelia cells reshapes into a tube. This neural tube is the precursor of the brain and the spinal cord [48]. In humans the process occurs during the third and fourth weeks of embryogenesis, when most women have just realized that they are pregnant. Due to the impracticalities of viewing human embryos at this early stage as well as the ethical issues, most studies of neurulation use animal models [11]. Images of neurulation in axolotl, the animal model used in this study, are shown in Figure 1.1.

During the formation of the neural tube, defects or groups of defects may occur that lead to incomplete neural tube closure. These groups of defects are generally referred to as *neural tube defects (NTDs)* [48]; two common types of NTDs are anencephaly and spina bifida [5, 8, 11]. In anencephaly, the portion of the neural tube that form the brain does not close properly resulting in the absence of major portions of the brain, skull and scalp. In spina bifida, the spinal cord is incompletely formed due to improper closure of the spinal cord portion of the neural tube. Anencephaly and some cases of spina bifida are fatal, while some infants with spina bifida survive as a result of extensive medical and surgical care [5, 11]. A long term study of 117 open spina bifida patients showed a mortality rate of 51% [31]. The 57 survivors ranged in age from 26 to 33; of the survivors 21 live

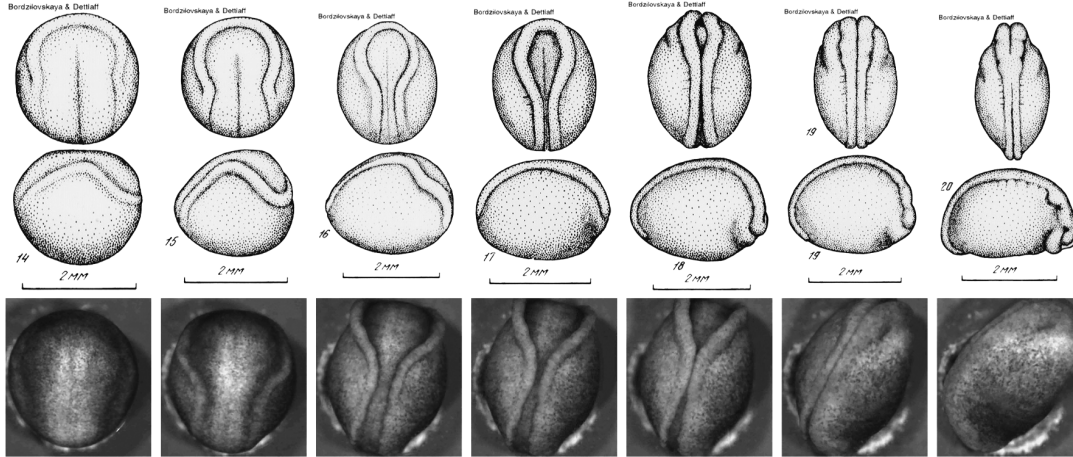


Figure 1.1: The neurulation of an axolotl embryo. (top) Sketches from [1]. (bottom) Time-lapse images obtained from the Frogatron 3000 robotic microscope [52].

independently, 17 need some support and 19 need daily care [31].

NTDs are the most common cause of human malformations (birth defects) and their occurrence varies largely between different populations [5, 11, 48]. In the low-risk Finnish population the occurrence is 1 in 3000 while in the high-risk areas of Ireland and UK the occurrence is 1 in 300 [48]. Studies have shown genetic, environmental and dietary influences for the cause of NTDs [5, 8]. There has also been evidence that consumption of sufficient amounts of vitamin B folic acid can prevent NTDs [5]. However, the fundamental embryonic mechanism responsible for the development of the neural tube and the cause of NTDs is still not known [11].

Personnel at the Embryo Biomechanics Lab (EBL) at the University of Waterloo study the internal forces and mechanisms that cause embryo development, in order to learn about the possible mechanisms of NTDs. Using images of embryo development [52], measurements of the tensile properties of embryo epithelial [54] and finite element models [6, 10], the stresses and strains within the developing embryo have been quantified [3].

Computer simulations have shown that the frequency and direction of mitosis can cause internal forces that drive embryo epithelia deformation [7]. For example, EBL has shown that in simulated embryo epithelia, mitosis normal to the major axis of the elliptical cells results in isotropic tissue growth whereas embryo epithelia that undergo vertically aligned mitosis grow in the vertical direction (Figure 1.2) [7]. However, these simulations can not show what fraction of the internal forces present during embryo development are caused by mitosis.

To determine the extent of internal forces that are caused by mitosis, the frequency and orientation of mitosis on the embryo epithelia must be identified. Time-lapse images of embryo epithelia sections (Figure 1.3), obtained from the Frogatron 3000 robotic microscope [52], can be used to quantify mitosis. Once quantified, these data can be used to determine the forces that are generated within the embryo

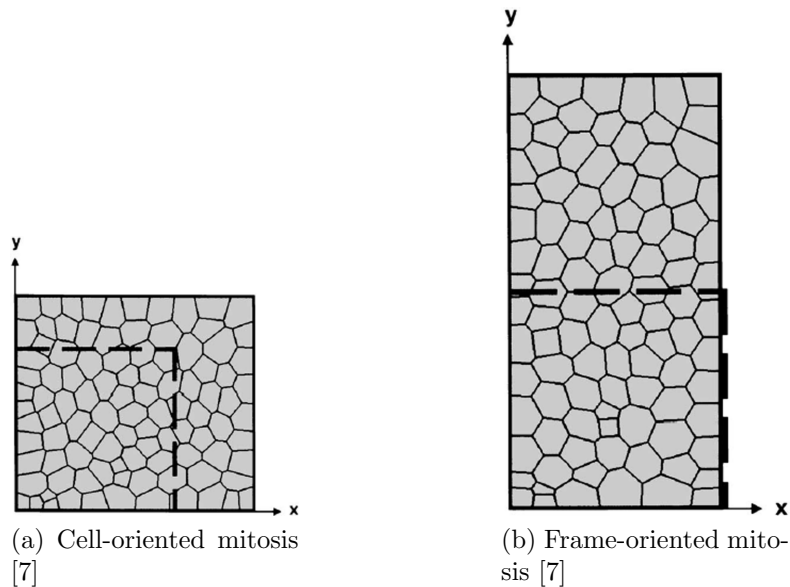


Figure 1.2: (a) In cell-oriented mitosis the original embryo epithelia (dashed box) undergoes simulated mitosis in which all mitosis occurred along a normal to the major axis of the elliptically modeled cells; this results in isotropic tissue growth. (b) In frame-oriented mitosis the original embryo epithelia (dashed box) undergoes mitosis along the vertical axis; this results in vertical tissue growth.

epithelia as a result of mitosis. However, manual counting of mitosis in time-lapse images of embryo development is tedious, time consuming and not reliable. As a result, to develop an automated image processing algorithm to quantify mitoses in image sequences of embryo epithelia is desirable.

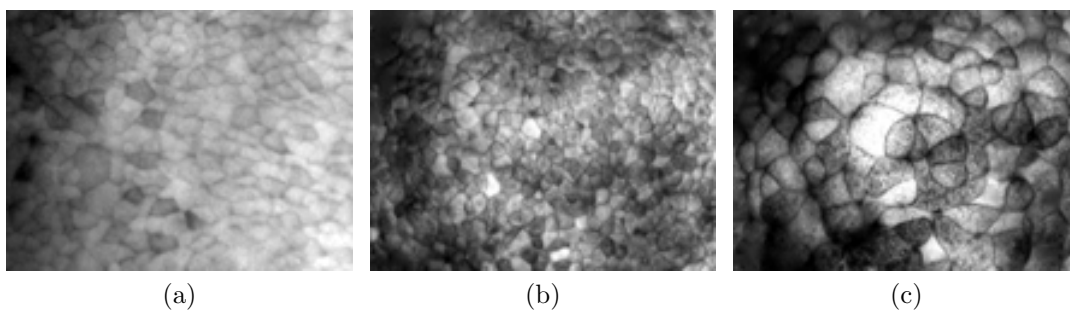


Figure 1.3: Some images of embryo epithelia with varying lighting conditions and cell sizes where mitosis are to be detected.

Existing methods for automatic detection of mitosis rely on counting cells by segmenting individual cells or identifying nucleus division on chemically stained tissue segments (Chapter 2). However, for the embryo epithelia images these approaches are not suitable due to poor image quality and the need observe embryo development that is not influenced by any external chemicals. As a result of these

limitations associated with existing mitosis identification methods, new methods are developed for the identification of mitosis in embryo epithelia.

In this study, unlike most previous studies, time-lapse images of embryos are used. As a result temporal information of the cell lattice is available. Using the temporal information, this thesis presents two new methods of mitosis detection in embryo epithelia. The first method (Chapter 3), determines mitosis locations using local motion patterns that are unique to mitoses. The second method (Chapter 4), determines mitosis locations by locating the intensity drops that occur during the nucleus division phase of mitoses.

The performance of the two proposed algorithms are then analyzed and compared on images of embryo epithelia with hand marked mitosis locations (Chapter 5). Conclusions and future works are then presented based on the algorithm analyzes (Chapter 6).

Chapter 2

Background

A single mitosis obtained from time-lapse images of embryo epithelia is illustrated in Figure 2.1. The duration of a mitosis $t_{Mitosis}$ is defined as the time in frames for the mother cell to divide into two daughter cells, starting at the frame before the cell boundaries start moving. The direction of mitosis $0 \leq \alpha_{Mitosis} \leq \pi$ is the angle measured counter-clockwise from the positive x-axis to the normal of the cell boundary formed between the two daughter cells. Finally, the time to nucleus division, $t_{NucleusDiv}$, is the time, in frames, from the start of mitosis to the start of nucleus division. The nucleus division is characterized by the dark spot or line along the width of the cell in frames 3 to 5.

Previous attempts at automatic and manual identification of mitosis can be categorized as cell counting approaches and nucleus division identification approaches. In cell counting approaches, the cells in each time-lapse image are counted and the mitosis count is then inferred from the increase in the number of cells; these methods are discussed in Section 2.1. In nucleus division identification approaches, time-lapse images are not used, instead mitosis are identified as locations in still images where nucleus division is present; these methods are discussed in Section 2.2.

2.1 Cell Counting

Cell counting methods [4, 9, 37, 41] were developed for cell cultures, not tissue segments, because in cell cultures individual cells are isolated on a uniform background allowing the use of computer vision segmentation algorithms to obtain a cell count. In embryos, the cells are joined together in a lattice network such that all cells are attached to multiple other cells. As a result, the segmentation algorithms used in [4, 9, 37, 41] can not be used for cell counting.

There have been several studies on segmenting cells in cell lattices of both organic and non-organic materials. One such study is used to segment and count tumor cells in cancer tissue segments [33]. In this study the cancer tissue segments are

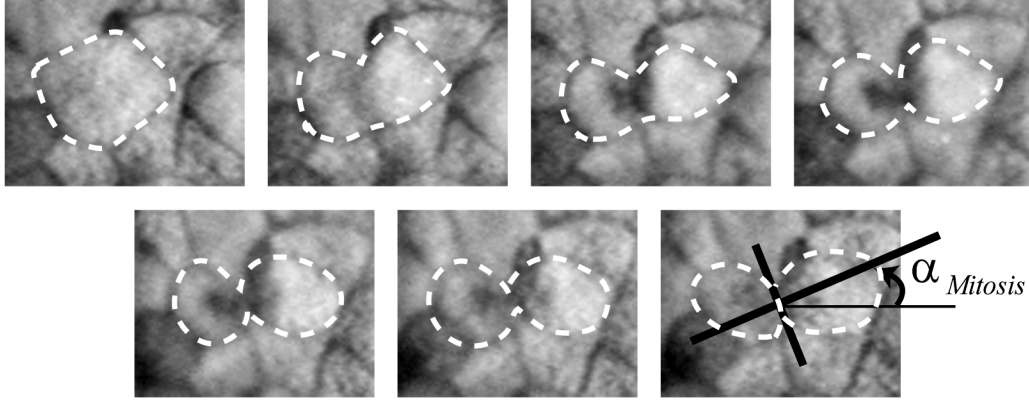


Figure 2.1: A single mitosis isolated from time-lapse images of embryo epithelia. Each frame is 5 min apart and mitosis orientation is defined by $\alpha_{Mitosis}$.

chemically stained such that there is a high contrast between tumor cells and non-tumor cells, as a result the tumor cells appear as dark spots on uniform non-tumor cell background (Figure 2.2a). Due to the low density of tumor cells, these images resemble images of cell cultures as opposed to images of tissue segments.

Another study looked at segmenting individual corneal cells from images of human cornea endothelial (Figure 2.2b). This work used a morphological preprocessing operator to obtain the center location of each corneal cell, then using this information with a watershed algorithm, individual corneal cells are segmented [53]. The morphological preprocessing operator relies on the high contrast of the boundaries in cornea endothelial to detect the centers of corneal cells. In the case of embryo epithelia, the high contrast cell boundary is not visible, reducing the performance of the morphological preprocessor. Furthermore, embryo epithelia are composed of cells separated by a dark boundary (line boundary) and adjacent cells with no visible boundary between them other than their intensity difference (edge boundary). Since the images of cornea endothelial contain only line boundaries, the morphological preprocessor works only for line boundaries.

In electron microscope (EM) images of non-organic materials, such as nickel, there are both line and edge boundaries (Figure 2.2c). In the study of these materials, there has been work done on identifying all cell boundaries by using the real and imaginary parts of the Gabor filter [46]. Due to focus defects, noise, and poor illuminations, the cell boundaries are not as readily visible in the embryo epithelia images as they are in the EM images. As a result, the method presented in [46] is not guaranteed to detect all cell boundaries and is thus not reliable to give sufficiently accurate cell counts for mitosis identification. An example of the cell boundary detection using [46] is illustrated in Figure 2.3.

Previous studies on embryo epithelia dealt with identifying average cell shape and size from images [25, 40]. A cell segmentation algorithm is developed in [25] for obtaining cell shape and size. This segmentation algorithm used local con-

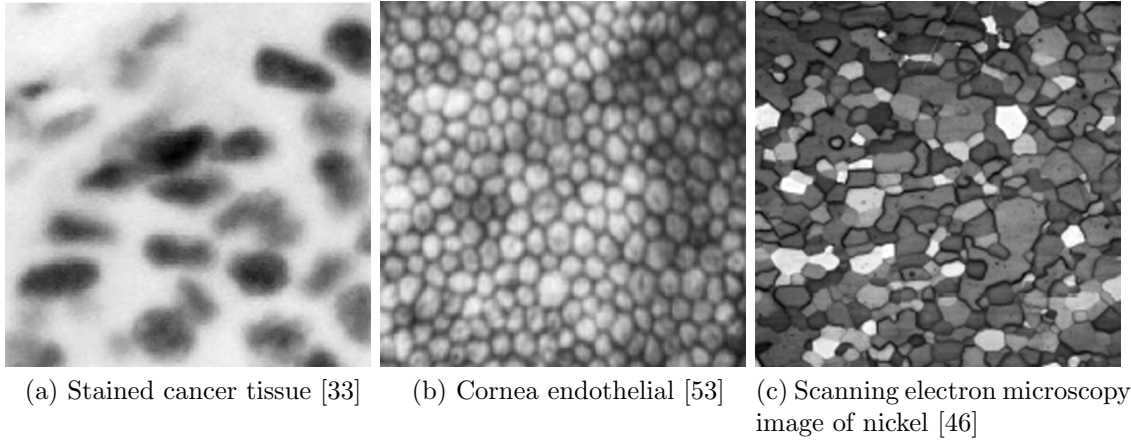


Figure 2.2: Images of different cell lattices where individual cells are to be segmented.

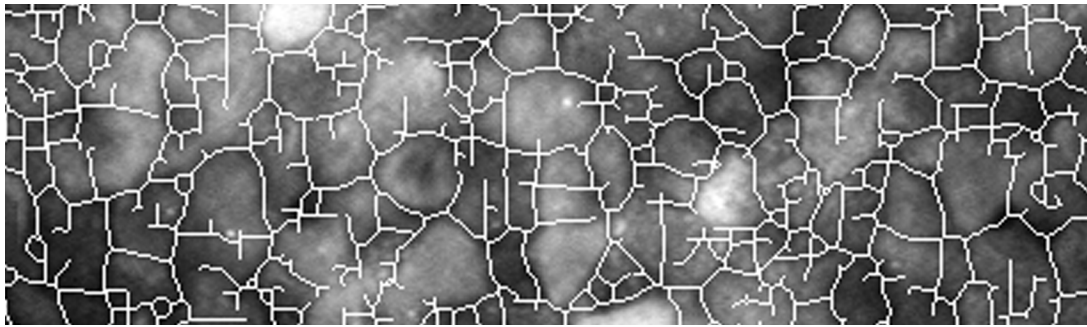


Figure 2.3: The cell boundaries in this image, marked by the white lines, were obtained using the real and imaginary Gabor filter responses [46]. The threshold on the Gabor filter response controls the number of boundary pixels returned; a lenient threshold will result in many false positive boundary pixels and a strict threshold will result in many false negative boundary pixels. Even with a very lenient threshold, allowing for many false positives, not all cell boundaries are detected as seen here.

trast enhancement followed by an iterative watershed algorithm. The analysis in [25] showed that segmentation of individual cells were difficult due to lack of cell boundary visibility. An example of the segmentation result from [25] is provided in Figure 2.4.

2.2 Nucleus Division Identification

The number of mitoses or the *mitotic count* has been used extensively in the analysis of tumor growth, in particular for breast cancer patients [12]. The mitosis count for tumor diagnosis is obtained from an image of fixed tissue samples that has been chemically stained. The cells on a breast cancer tissue segment undergoing mitosis

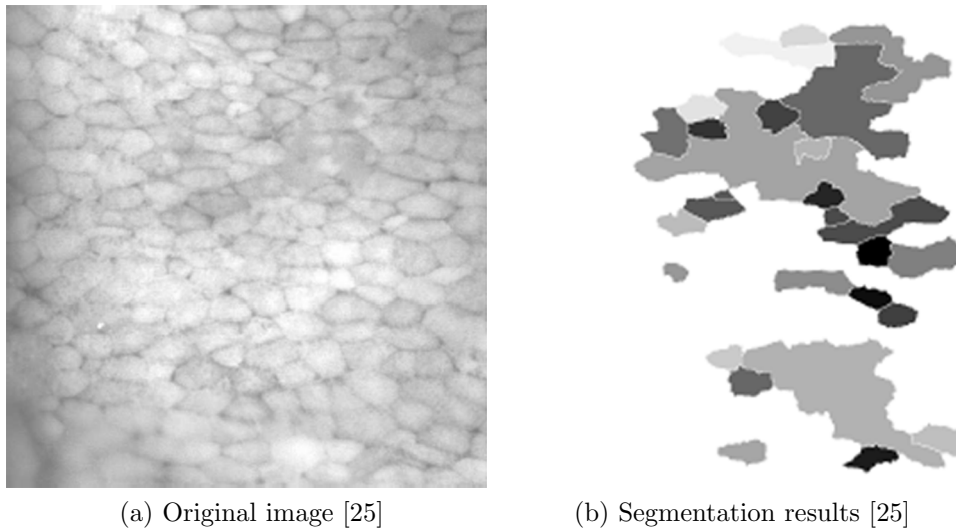


Figure 2.4: An example segmentation result of embryo epithelia using the segmentation algorithm presented in [25].

are recognized by the following description [43]:

- “Absence of nuclear membrane.”
- “Absence of a clear zone in the center.”
- “Presence of hairy projections.”
- “Presence of cytoplasm that is basophilic rather than eosinophilic.”

From an image processing perspective, the center of the cells undergoing mitosis appear as compact dark regions with hairy boundaries [27] as seen in Figure 2.5a. Most publications in this field address the issue of obtaining accurate mitotic count based on multiple manual counts of these dark regions [12, 20, 43, 50]. A feasibility study of an automated process for obtaining mitotic count was presented in [26].

The only automated algorithm for counting mitoses, in stained cancer tissue, was presented in [27]. This automated method used a threshold to obtain initial seeds of the dark regions. Using the seeds, a region growing algorithm was used to identify the total area of all potential mitosis regions. The identified regions were classified as mitosis using a Fisher linear discriminant. The features used for the classification of each region are the optical mass, average optical density, standard deviation of optical density, minimum gray value, a measure of homogeneity, area, parameter and the bending energy along the parameter.

This dark region, resulting from nucleus division, is also present in the axolotl images used in this study (Figure 2.5b). However, since the live embryo can not be chemically treated without altering its natural growth, the nucleus division points are not always the darkest spots on the embryo epithelial image; as a result the

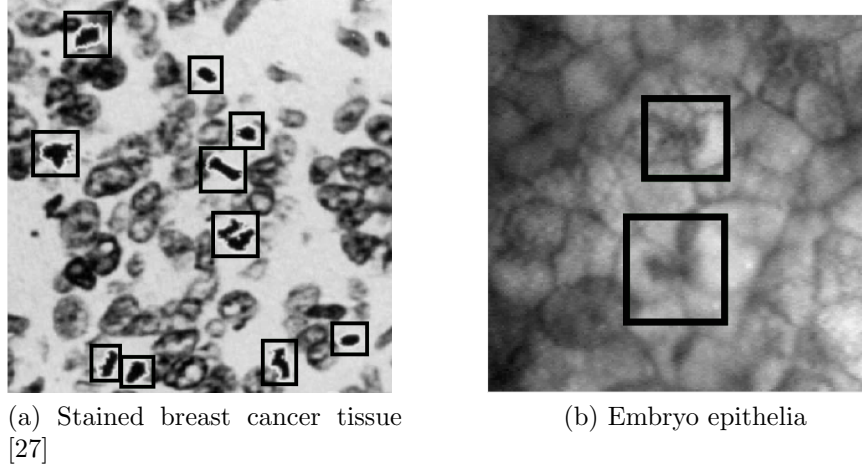


Figure 2.5: (a) Chemically stained breast cancer tissue sample [27] where the mitosis locations, during nucleus division, appear as dark regions with hairy boundaries. (b) Embryo epithelia where the mitosis locations, during nucleus division, appear darker but are not the darkest regions in the image.

automated algorithm presented in [27] can not be used for the analysis of embryo epithelia.

2.3 Tracking

To obtain temporal information from the time lapse images of embryo epithelia, concepts from visual tracking are used. Background information on the tracking scheme used in this thesis is presented here, along with the reasons for choosing this scheme. For a detailed explanation of visual tracking please refer to [24, 49, 55].

Yilmaz et al. [55] categorized tracking into point trackers, kernel trackers and silhouette trackers. Point trackers represent the object being tracked as a set of points. Kernel trackers represent the object as a geometric shape such as rectangle or ellipse. Silhouette trackers represent the object by its silhouette. Based on these three categories, for tracking embryo epithelia, the epithelia can be represented as a set of points, a set of ellipses representing individual cells in the epithelia or a set of silhouettes of individual cells in the epithelia (Figure 2.6).

Point trackers are further broken down into deterministic and probabilistic trackers [55]. Probabilistic methods, unlike deterministic methods, account for noise in the image as well as random perturbations of the object being tracked [55]. Two main algorithms for probabilistic based point trackers are Kalman filtering [49] and particle filtering [49]. In this work Kalman filtering is used because all noise in the system are assumed to be Gaussian.

A brief overview of the use of Kalman filter for tracking points on the epithelia is presented here. The Kalman filter will not be derived here and the reader is

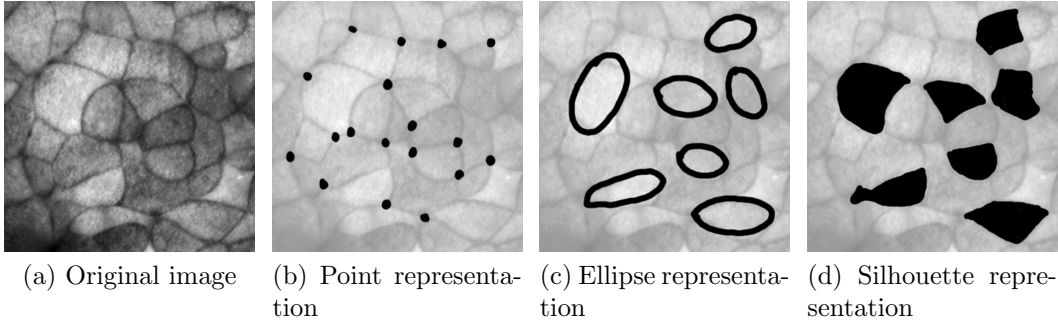


Figure 2.6: The epithelia to be tracked can be represented as a set of salient points or a set of ellipse representing individual cells or a set of silhouettes of individual cells. The number of points, ellipses and silhouettes can be varied.

referred to [49] for detailed investigation and derivation of the Kalman filter.

2.3.1 Dynamic Model

The goal of point trackers is to track the location of a point on the epithelia over several frames in an image sequence. The point on the epithelia is represented by a sequence of states \underline{z}_t and its corresponding covariance \mathbf{P}_t where $t = 0, 1, 2, \dots$ is the frame number. The dynamics of the states are modeled to be

$$\begin{aligned} \underline{z}_t &= \mathbf{A}_t \underline{z}_{t-1} + \underline{w}_t \\ \underline{w}_t &\sim \mathcal{N}(\underline{0}, \mathbf{R}) \end{aligned} \quad (2.1)$$

where \mathbf{A}_t is the model parameter and \underline{w}_t is the noise in the dynamic model; this noise is called the process noise. The process noise is assumed to be zero mean Gaussian noise with variance \mathbf{R} .

Observation and experimental study demonstrated that points on the epithelia can be modeled as having both a constant velocity and a linear motion between frames because very little motion occurs between frames. In this case the state can be represented using the location (x, y) and velocity $\vec{v} = (v_x, v_y)$ of the point at each frame ($\underline{z}_t = [x \ y \ v_x \ v_y]^T$). The model parameter \mathbf{A}_t is constant for each frame t and is defined as

$$\mathbf{A}_t = \mathbf{A} = \begin{bmatrix} 1 & 0 & \Delta t & 0 \\ 0 & 1 & 0 & \Delta t \\ 0 & 0 & 1 & 0 \\ 0 & 0 & 0 & 1 \end{bmatrix} \quad (2.2)$$

where Δt is the time between two consecutive frames. If the velocity is represented as pixels per frame then $\Delta t = 1$.

2.3.2 Measurement Model

In addition to the dynamic model of the points on the epithelium, the state of the point can be measured at each frame. The measurement \underline{m}_t of the state is related to the true state \underline{z}_t as

$$\begin{aligned}\underline{m}_t &= \mathbf{C}_t \underline{z}_t + \underline{v}_t \\ \underline{v}_t &\sim \mathcal{N}(\underline{0}, \mathbf{Q}_t).\end{aligned}\tag{2.3}$$

\underline{v}_t is the zero mean Gaussian noise in the measurement and \mathbf{C}_t is the relationship between the measured state and the true state. In this study, only the location (x, y) of the point being tracked is measured at each frame. Therefore,

$$\mathbf{C}_t = \mathbf{C} = \begin{bmatrix} 1 & 0 & 0 & 0 \\ 0 & 1 & 0 & 0 \end{bmatrix}.\tag{2.4}$$

There are many methods for obtaining the measurement \underline{m}_t [55]. The simplest method is the normalized cross-correlation between frames of a local region of interest (ROI) around the point being tracked [51]. Another method is the phase disparity measure [18] in a local N by N neighborhood. Based on a study of tracking 20 points over 18 frames on an epithelium, it was found that the phase disparity measure [18] is more accurate than the correlation method. However, the correlation method is computationally faster than the phase disparity measure. For tracking the 20 points, the phase disparity measure had a mean error of 4.9 pixels with a standard deviation (std.) of 3.6 where as the correlation method had a mean error of 11.0 pixels with a std. of 13.0 pixel.

To obtain the phase disparity measure a Gabor filter bank is used [18]. For each of the filter in the filter bank the phase at each point being tracked is obtained as:

$$\phi = \arctan \frac{Im}{Re}\tag{2.5}$$

where Im is the imaginary response of the Gabor filter and Re is the real response of the Gabor filter. The phase disparity between two phase measurements are obtained as [18]:

$$disp(\phi_1, \phi_2) = \frac{[\phi_1 - \phi_2]_{2\pi}}{0.5(\phi'_1 + \phi'_2)}\tag{2.6}$$

where ϕ'_1, ϕ'_2 are the first derivatives and $[\phi]_{2\pi}$ denotes a cyclic difference, i.e. $[\phi]_{2\pi} \in (-\pi, \pi]$.

Given A_ϕ^ω ($\phi = -45^\circ, 0^\circ, 45^\circ, 90^\circ$ and $\omega = 0.5, 1, 1.5$ line width) the phase responses at frame t , B_ϕ^ω the phase responses at frame $t + 1$, a search area size N ,

the point (x, y) to be tracked and the dynamic model prediction of that point on the next frame $(\hat{x}^{DM}, \hat{y}^{DM})$, the phase disparity measure is outlined in Algorithm 2.3.2. The result of the matching process is the measured location \underline{m} of point (x, y) and its corresponding covariance matrix \mathbf{Q} . The constant k used in Algorithm 2.3.2 was obtained by studying the phase disparity values. To effectively use the phase disparity measure the point being tracked must be a triple junction point (TJP) or a cell boundary point; numerical issues, such as divide by zero, occur when the point is in a uniform area such as the center of a cell.

Algorithm 1 Obtain Phase Disparity Measurement

$\hat{x} = \hat{x}^{DM}$, DM - Dynamic Model
 $\hat{y} = \hat{y}^{DM}$
 $\omega_{array} = [1.5 \quad 1 \quad 0.5]$
 $i, j = -\frac{N-1}{2}, \dots, \frac{N-1}{2}$
 $k = 5$ Obtained experimentally
for $n = 0$ to 2 **do**
 $\omega = \omega_{array}(n)$
 $D^\omega(i, j) = \frac{1}{4} \sum_{\phi} disp(A_{\phi}^{\omega}(x, y), B_{\phi}^{\omega}(\hat{x} - i, \hat{y} - j))$
 $\Re = e^{-kD^\omega}$
 $\Delta x = \frac{1}{\sum_{i,j} \Re(i, j)} \left(\sum_{i,j} \Re(i, j) i \right)$
 $\Delta y = \frac{1}{\sum_{i,j} \Re(i, j)} \left(\sum_{i,j} \Re(i, j) j \right)$
 $\hat{x} = \hat{x} + \Delta x$
 $\hat{y} = \hat{y} + \Delta y$
end for
 $\underline{m} = (\hat{x}, \hat{y})$
 $\mathbf{Q} = \frac{1}{\sum_{i,j} \Re(i, j)} \begin{bmatrix} \sum_{i,j} \Re(i, j) (i - \Delta x)^2 & \sum_{i,j} \Re(i, j) (i - \Delta x) (j - \Delta y) \\ \sum_{i,j} \Re(i, j) (i - \Delta x) (j - \Delta y) & \sum_{i,j} \Re(i, j) (j - \Delta y)^2 \end{bmatrix}$

2.3.3 Kalman Filtering

The Kalman filter [49, 55] recursively estimates the true state of a point at frame t given the dynamic model and the measurement model. The three steps in Kalman filtering are prediction, measurement and update.

In the prediction step the dynamic model (Eq. 2.1) is used to estimate the current state given the previous state, $\hat{\underline{z}}_{t|t-1}$, and its covariance $\mathbf{P}_{t|t-1}$ as [49, 55]:

$$\hat{z}_{t|t-1} = \mathbf{A}\hat{z}_{t-1|t-1} \quad (2.7)$$

$$\mathbf{P}_{t|t-1} = \mathbf{A}\mathbf{P}_{t-1|t-1}\mathbf{A}^T + \mathbf{R} \quad (2.8)$$

where $\hat{z}_{t-1|t-1}$ is the previous state estimated by the Kalman filter and $\mathbf{P}_{t-1|t-1}$ is the previous covariance estimated by the Kalman filter. For the recursion, the initial conditions needed are $\hat{z}_{0|0}$ and $\mathbf{P}_{0|0}$ where $\hat{z}_{0|0}$ is the state at frame 0 and $\mathbf{P}_{0|0}$ is the covariance of the state at frame 0.

In the measurement step the current state \underline{m}_t and its covariance \mathbf{Q}_t are obtained from the measurement model.

In the update step, the predicted state $\hat{z}_{t|t-1}$ and the measured state \underline{m}_t are combined using the Kalman gain \mathbf{K}_t to obtain an estimate of the true state at the current frame $\hat{z}_{t|t}$ and its covariance $\mathbf{P}_{t|t}$ as [49, 55]:

$$\mathbf{K}_t = \mathbf{P}_{t|t-1}\mathbf{C}^T(\mathbf{C}\mathbf{P}_{t|t-1}\mathbf{C}^T + \mathbf{Q}_t)^{-1} \quad (2.9)$$

$$\hat{z}_{t|t} = \hat{z}_{t|t-1} + \mathbf{K}_t(\underline{m}_t - \mathbf{C}\hat{z}_{t|t-1}) \quad (2.10)$$

$$\mathbf{P}_{t|t} = \mathbf{P}_{t|t-1} - \mathbf{K}_t\mathbf{C}\mathbf{P}_{t|t-1} \quad (2.11)$$

To illustrate the performance of the Kalman filter estimate over direct measurement estimate, consider a simulated 1D translation where the state is represented as $\underline{z}_t = [x \ v_x]^T$ and $\underline{z}_0 = [0 \ 10]$. For this 1D case 100 frames were simulated using Eq. 2.1 with $\mathbf{R} = 4\mathbf{I}$ and $\mathbf{A} = \begin{bmatrix} 1 & 1 \\ 0 & 1 \end{bmatrix}$. The position measurements were also simulated using Eq. 2.3 with $\mathbf{C} = [1 \ 0]$ and Q_t randomly selected from the distribution $\mathcal{N}(0, 1000)$. Note that since Q_t is a variance, the absolute value of the randomly selected numbers are used. Having simulated the ground truth \underline{z}_t , measurements \underline{m}_t and measurement variance Q_t for 100 frames, the Kalman filter was used to obtain the estimated position and velocity.

To apply the Kalman filter, the initial condition of the state was chosen as $\hat{z}_{0|0} = \underline{z}_0$ and $\mathbf{P}_{0|0} = 100\mathbf{I}$. The process noise variance was chosen as $\mathbf{R} = \mathbf{I}$; this value is different than the process noise variance used to simulate ground truth because in a real world application the true process variance is not known.

The position result of the Kalman filter at time $t = 95$ is given in Figure 2.7. From the probability density function (pdf) of the predicted location, measured location, and estimated true location (Figure 2.7), it can be seen that the estimated location lies between the predicted and measured locations and its confidence is higher than the confidence of predicted and measured locations as seen by the smaller variance of the estimated location. By plotting the variance of the estimated location $\mathbf{P}_t(1, 1)$ and the measured location Q (Figure 2.8) it can be seen that the estimated location variance quickly converges from the initial condition of 100

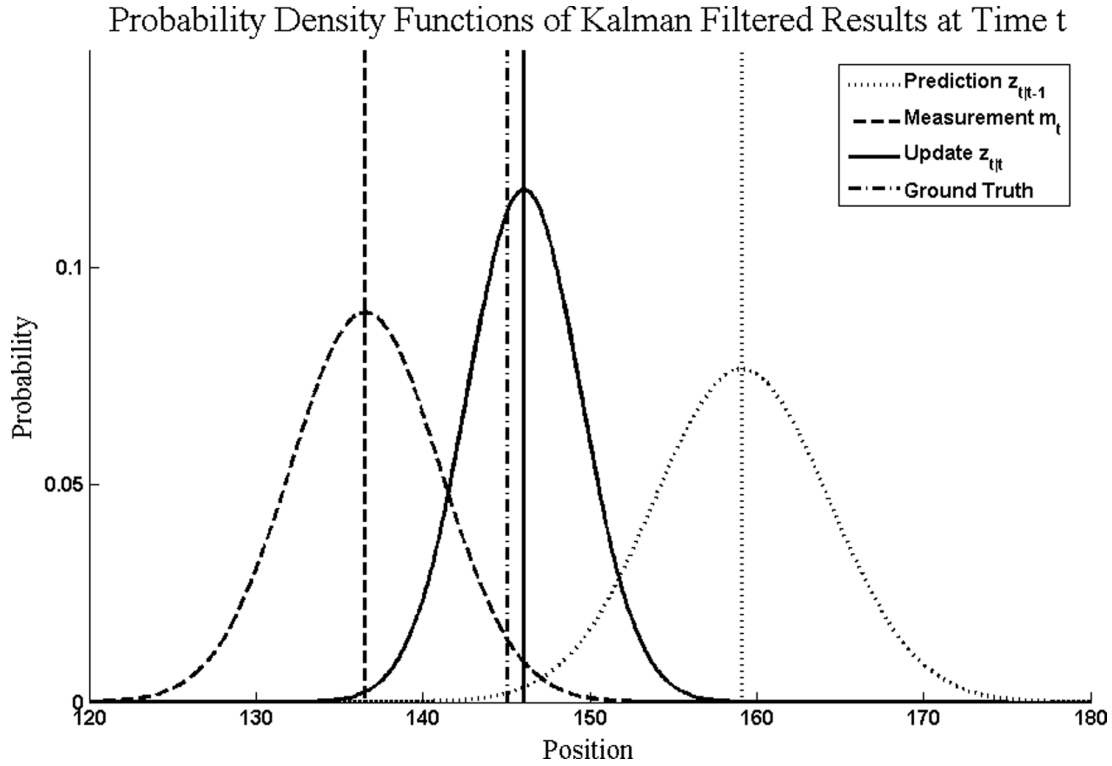


Figure 2.7: The Kalman filtering result at $t = 95$ for 1D translation. The vertical lines represents the predicted, measured, updated and ground truth location of the point being tracked. Around each of the predicted, measured and updated locations is the pdf of the location; the higher the confidence in the location, the narrower the pdf of that location. It is important to note that sometimes the location of the prediction or measurement will be closer to the ground truth than the update location, however, the confidence of the updated location will always be higher than the predicted and measured location.

to a mean confidence value of approximately 9 even though the variance of the measurement is not converging.

The mean absolute error between the measured location and the ground truth over the entire 100 frames is 3.72 with a standard deviation of 3.67. The mean error between the Kalman filter estimate and the ground truth is 2.75 with a standard deviation of 2.55.

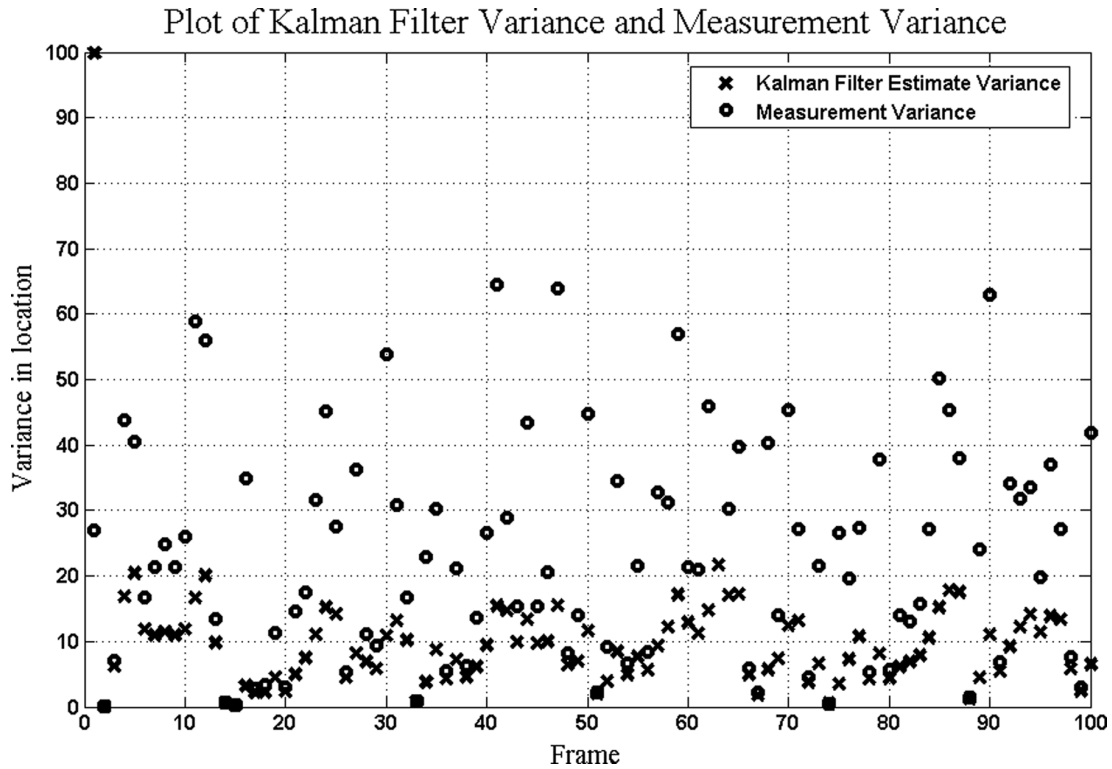


Figure 2.8: When comparing the variance of the Kalman filter estimate of the point being tracked to that of the measurement estimate, the variance of the Kalman filter estimate is on average smaller than the measurement variance. Furthermore, the initial large estimate of the state variance drops to a much smaller value after the first time step.

Chapter 3

Motion Based Algorithm

Image sequences in which mitoses occur (Figure 3.1) show that distinctive motion patterns accompany this process. Inward motion (see points marked with a $+$) occur along the newly formed cell boundary and outward motion (see points marked with a \circ) occurs along an axis through the daughter cells. These motions are approximately normal to each other and are consistent with those predicted by computer simulations [7]. The third and final pattern is the outward motion (see points marked with a $*$) caused by the growth of the nucleus region. Using these motion patterns, mitoses in time lapse images of embryo epithelia will be identified.

The overall scheme for identifying mitoses through local motion fields is presented in Figure 3.2. First the distinctive motion patterns that occur during mitoses are combined to produce a *mitosis motion field prototype* (Section 3.1). Next the motion field of all images in the time lapse image sequence are identified (Section 3.2). Once the image motion fields are calculated, the *mitosis motion field prototype* is matched within the image motion fields (Section 3.3). Thresholds can then be applied to the result of the matching process to obtain a mitosis count (Section 3.4).

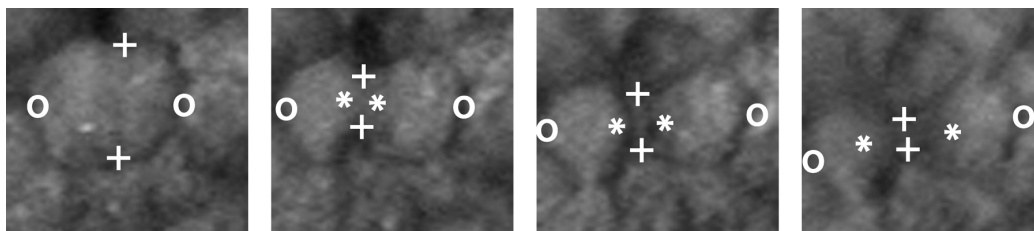


Figure 3.1: A single mitosis obtained from time-lapse images of embryo epithelia. The key motion patterns within a single mitosis are marked up with the symbols $+$ (inward motion), \circ (outward motion) and $*$ (nucleus region motion).

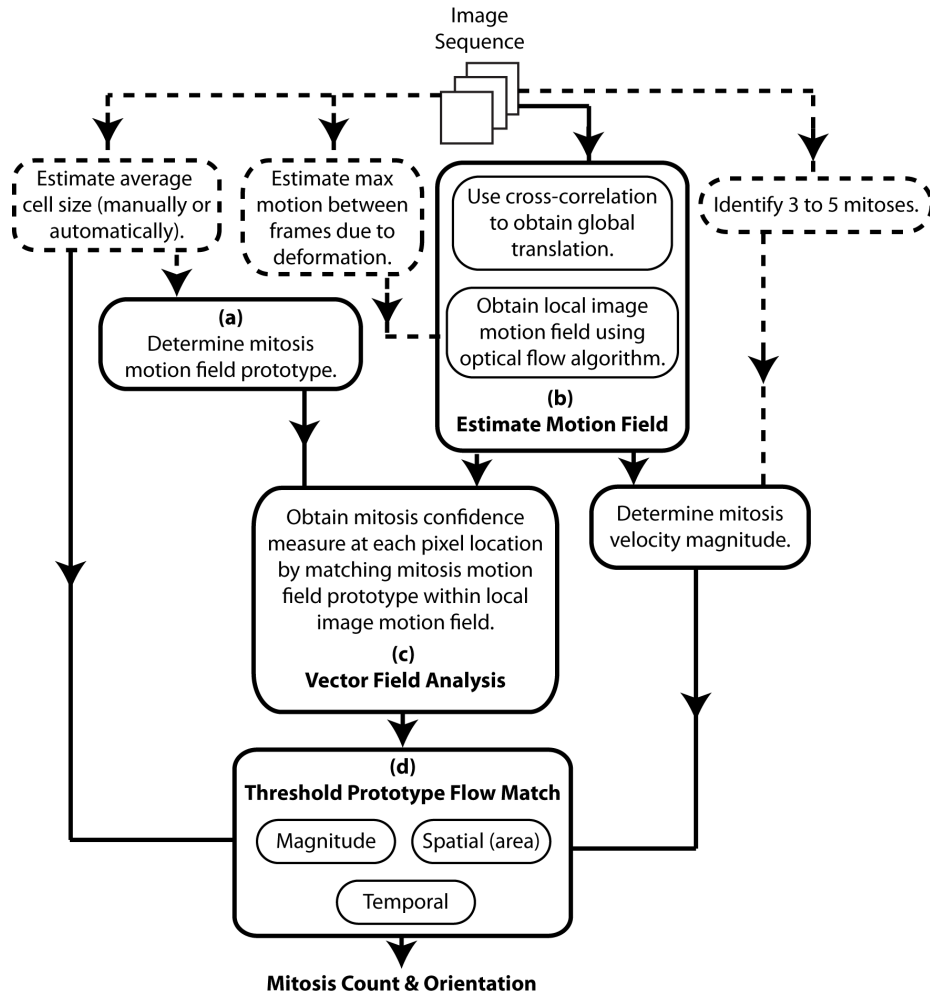


Figure 3.2: Overview of the motion based algorithm for mitosis detection. This algorithm detects mitoses by matching the *mitosis motion field prototype* within the local image motion field. The dashed boxes represents parameters that are needed by the algorithm and must be estimated by the user. (a) A *mitosis motion field prototype* is developed based on observations and simulations. (b) Local image motion field is estimated using optical flow, after all global translational motions have been removed. (c) The *mitosis motion field prototype* is matched within the image motion field using both orientation and magnitude of the velocity vectors. (d) Magnitude, area and temporal thresholds are applied to the motion field prototype matches to obtain mitosis count and orientation.

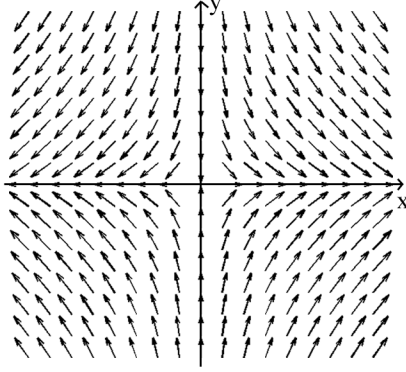


Figure 3.3: The motion field representing the template motion that occurs during a single mitosis. This motion field will be referred to as the *mitosis motion field prototype*.

3.1 Mitosis Motion Field Prototype

These three motion patterns, identified in Figure 3.1, can be combined into a single motion field model as illustrated in Figure 3.3. This motion field model will be referred to as the *mitosis motion field prototype*, and can be described mathematically as a saddle point $\mathcal{V}(\underline{x})$, using the vector field equation [42]

$$\mathcal{V}(\underline{x}) = \mathbf{A}\underline{x} + \underline{b}, \quad (3.1)$$

where \underline{x} is a point on the prototype coordinate system (Figure 3.3) and $\underline{b} = [0 \ 0]^T$ is the offset of the vector field pattern from the origin. To represent a saddle point, \mathbf{A} must be chosen such that its eigenvalues are real and the product of the eigenvalues is less than zero [42].

By observing the flow patterns of mitoses image sequences it was found that the saddle point created by $\mathbf{A} = \begin{bmatrix} -1 & 0 \\ 0 & 1 \end{bmatrix}$ is a fair approximation for most mitosis. In some image sequences, the inward motion illustrated by $+$ in Figure 3.1 is not dominant when compared to the other two motion patterns. In these cases $\mathbf{A} = \begin{bmatrix} -1 & 0 \\ 0 & 100 \end{bmatrix}$ was found to be a more suitable choice. The two values of \mathbf{A} used in this study does not represent all saddle points but do represent many of the mitoses patterns that were observed by the author. Nevertheless, when using these prototypes small deviations from these two saddle points must be allowed.

Having defined the *mitosis motion field prototype*, the task of detecting mitosis is the same as finding all occurrences of this prototype in the motion field of the time-lapse images.

3.2 Image Motion Field

Identification of the *mitosis motion field prototype* is complicated by the fact that the epithelia that cover the surface of an embryo undergo stretching, reshaping, and translation as the embryo develops. In this study the total epithelia motion (\mathcal{U}) will be modeled as

$$\mathcal{U} = \mathcal{L} + \vec{T} \quad (3.2)$$

where \mathcal{L} , also referred to as the local image motion field, is the local deformation field caused by mitoses and \vec{T} is the global translation of the epithelia in the camera view. A more detailed model would incorporate a large-scale reshaping field \mathcal{R} in addition to the local deformation and global translation. In high-magnification images, like those of interest here, image translation dominates large-scale reshaping and thus large-scale reshaping is ignored in this study.

In order to detect the *mitosis motion field prototype* in the local image motions field \mathcal{L} , the global translation \vec{T} must be removed. A variety of image registration methods are available for estimating global translation between two image frames [29]. The simplest of these methods, the normalized cross-correlation between frame t and $t + 1$, performs well for pure translations and cases where intensities between frames are constant. Since the images used here have fairly uniform illumination between frames and only pure translation information needs to be recovered, the normalized cross-correlation is used to estimate the global translation between the two frames. The translation is then removed by translating frame $t + 1$ by $-\hat{\vec{T}}$.

Once the global translation between all frames in the image sequence is removed, an estimate of the local image motion field $\hat{\mathcal{L}}$ can be obtained using optical flow, “the distribution of apparent velocities of movement of brightness patterns in an image” [23]. Many methods are available for obtaining optical flow from image sequences [2]. Barron et. al. [2] categorized these methods into differential, region matching, energy and phase based techniques. Due to noise and grainy pigmentation of the epithelium, differential based techniques perform poorly. Energy and phase based techniques do not detect intensity changes caused by the nucleus division as motion (see points marked with a * in Figure 3.1) because these techniques are robust to illumination changes. Region matching techniques perform better than differential based techniques under noise and they also detect the intensity changes caused by the nucleus division, as a result a region matching optical flow algorithm is used to estimate the local image motion field $\hat{\mathcal{L}}$. The region matching optical flow algorithm used is a modified version of Singh’s optical flow algorithm [44]. Refer to Appendix A for details on the optical flow algorithm.

3.3 Motion Field Analysis

Having obtained the estimate of the local image motion field $\hat{\mathcal{L}}$, the task now is to find all occurrences of the *mitosis motion field prototype* in the local image motion field. Two standard approaches to analyzing vector fields are critical point analysis [36, 42] and template matching [15, 22]. In critical point analysis, locations of zero velocities are identified and categorized based on flow pattern around the zero velocity point. In template matching, a user-given template motion field pattern is matched within a larger motion field.

In this study, the template matching scheme is used because critical point analysis works best on dense vector fields; the vector fields estimated using optical flow are not dense fields. The template matching schemes [15, 22] only match orientation pattern as velocity magnitudes will differ from application to application. As a result the probability of mitosis at image location (i, j) , $\mathbf{P}_{Mitosis}(i, j)$, is determined as

$$\mathbf{P}_{Mitosis}(i, j) = \frac{\mathbf{P}_{VelOri}(i, j) + \mathbf{P}_{VelMag}(i, j)}{2}. \quad (3.3)$$

Where \mathbf{P}_{VelOri} is the velocity orientation weight determined by matching the *mitosis motion field prototype* within the image motion field and \mathbf{P}_{VelMag} is the velocity magnitude weight determined by analyzing the velocities near mitosis.

3.3.1 Velocity Orientation Weight

To obtain \mathbf{P}_{VelOri} , the template matching method defined by Heiberg [22] is used in this study; this method is the same as the zeroth order Clifford's Convolution [15]. The matching scheme is the dot product of the normalized template vector field within the normalized image motion field. The mean of the dot product for all pixels within the template window is used as the degree of the match. Thus the degree of match

$$\mathbf{D}(i, j) = \frac{1}{n^2} \sum_{x, y = -(n-1)/2}^{(n-1)/2} \hat{\mathcal{L}}(i-x, j-y)^T \mathcal{V}(x, y) \quad (3.4)$$

where $\mathbf{D}(i, j)$ is the degree of match at image location (i, j) , $\hat{\mathcal{L}}$ is the estimate of the local image motion field, \mathcal{V} is the template motion field and n is the size of the template. The template used is the previously described *mitosis motion field prototype*. The size of the template is chosen as the length of the minor axis of the average elliptical cell in the image. The average elliptical cell in the image can be determined using [25] or provided manually.

Since mitosis can occur at any orientation, templates at all possible rotations from 0° to 360° needs to be used. However, two templates with very small orientation difference will have similar match within the image motion field, since there is very little difference between the templates. Therefore template orientation increments of 5° was chosen as the trade off point between the need for exact orientation information and having two templates with the same match response.

At each location on the image motion field, the maximum dot product is kept as the degree of match and the orientation of the template is kept as the orientation of the mitosis. The maximum degree of match, \mathbf{D}_{MAX} , is then weighted using a sigmoid function to determine \mathbf{P}_{VelOri} ,

$$\mathbf{P}_{VelOri}(i, j) = \frac{1}{1 + e^{-k_{VelOri}(\mathbf{D}_{MAX}(i,j)+b_{VelOri})}} \quad (3.5)$$

where $k_{VelOri} = 5$ and $b_{VelOri} = 0.5$ were obtained experimentally.

3.3.2 Velocity Magnitude Weight

From observations on the data, the velocity magnitude of the mitosis is generally larger than the velocity magnitude of tissue deformations. That is, a high velocity magnitude is expected at mitosis locations. As a result \mathbf{P}_{VelMag} is obtained as the sigmoid weighted version of the velocity magnitude.

$$\mathbf{P}_{VelMag}(i, j) = \frac{1}{1 + e^{-k_{VelMag}(\|\hat{\mathcal{L}}(i,j)\|_{Smoothed}+b_{VelMag})}} \quad (3.6)$$

The magnitude of the local image motion field is smoothed using a uniform average filter of size n where n is the size of the *mitosis motion field prototype*; this will remove any noise in the velocity magnitudes. The parameters k_{VelMag} and b_{VelMag} are highly dependent on the image sequence and they are selected based on the data.

To select the values of k_{VelMag} and b_{VelMag} , some mitosis in the image sequences must be hand marked. A histogram of the smoothed local image motion field velocity magnitude at these hand marked mitosis location must then be constructed. Based on this histogram the value of b_{VelMag} is chosen as the minimum velocity found on the histogram; this will ensure that the minimum velocity of the mitosis region is assigned a weight of 0.5 on a 0 to 1 range. The value of k_{VelMag} is chosen such that $\mathbf{P}_{VelMag} = 1$ at the maximum velocity found on the histogram; this will ensure that the maximum velocity of the mitosis region gets the maximum weight. An example of the sigmoid weighting function and velocity histogram, created from five hand marked mitosis locations, is illustrated in Figure 3.4.

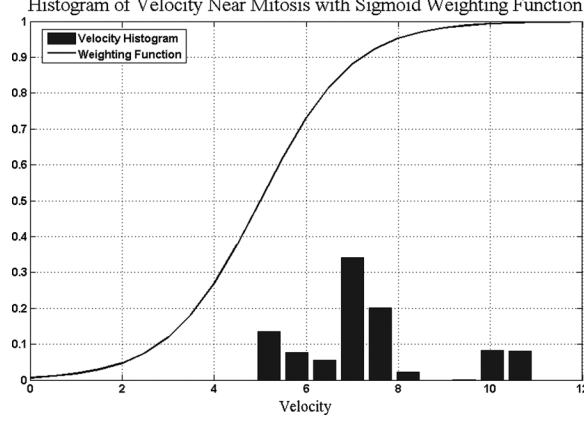


Figure 3.4: The velocity weighting sigmoid function is overlaid with the velocity magnitude histogram obtained from five hand marked mitosis locations. The sigmoid function parameter $b_{VelMag} = 5$, the smallest velocity in the histogram and $k_{VelMag} = 1$ to ensure that sigmoid function is at 1 for the maximum velocity in the histogram.

3.4 Mitoses Count and Orientation

The probability of mitoses at all image locations $\mathbf{P}_{Mitosis}$ has been obtained from the image motion field orientation and magnitude patterns. In order to obtain a discrete count of mitosis, thresholds need to be applied on $\mathbf{P}_{Mitosis}$ to locate all instances of high $\mathbf{P}_{Mitosis}$. Two magnitude thresholds T_{LOW} , T_{HIGH} and a spatial size threshold T_{SIZE} are used on $\mathbf{P}_{Mitosis}$.

The threshold T_{LOW} is first applied to obtain $\mathbf{P}'_{Mitosis}$, a binary image where all potential mitosis locations are indicated by the high pixels. To apply the spatial size threshold, a list \mathcal{C} of all 8-connected objects in $\mathbf{P}'_{Mitosis}$ is obtained. The 8-connected object, also known as the 8-connected component, is the set of all foreground pixels connected together using the eight-connectivity rule [21]. Refer to Appendix B for details on various pixel connectivity rules.

The size threshold T_{SIZE} is applied along with T_{HIGH} on each individual 8-connected object, $\mathcal{C}(i)$, as follows:

$$\mathbf{P}''_{Mitosis}(\mathbf{P}_i) = \begin{cases} 1 & \text{if } size(\mathbf{P}_i) > T_{SIZE} \parallel \max(\mathbf{P}_{Mitosis} \in \mathbf{P}_i) > T_{HIGH} \\ 0 & \text{Otherwise.} \end{cases} \quad (3.7)$$

where \mathbf{P}_i is a list of all pixels in the 8-connected object $\mathcal{C}(i)$; that is an 8-connected object remains a valid mitosis location if its size in pixel is larger than T_{SIZE} or a pixel in that object has a $\mathbf{P}_{Mitosis}$ value greater than T_{HIGH} . A morphological closing operator [14] with square structuring element of size N is performed on $\mathbf{P}''_{Mitosis}$ to connect any small gaps in $\mathbf{P}''_{Mitosis}$ as a result of the thresholds. The

value of $N = 7$ is used; this value will always be small. If a large value of N is used multiple mitosis will be joined as a single mitosis.

The number of mitoses are then obtained as the number of 8-connected objects in $\mathbf{P}''_{Mitosis}$. To avoid multiple detection of the same mitosis on different frames, any detected object in $\mathbf{P}''_{Mitosis}$ that spatially overlaps between consecutive frames are considered as the same mitosis. A single mitosis has many orientation estimates since it will have more than one pixel in the 8-connected object. Therefore the mitosis orientation estimation is obtained as the most commonly occurring orientation angle in the 8-connected object.

A method based on the image data for selecting thresholds T_{LOW} and T_{HIGH} is not available. They may vary between image sets, however, T_{LOW} and T_{HIGH} do depend on the sigmoid function parameters k_{VelOri} , b_{VelOri} , k_{VelMag} and b_{VelMag} . If the sigmoid function parameters are chosen well, that is they separate the mitosis pixels from non-mitosis pixels, then $T_{LOW} \approx 0.5$ and $T_{HIGH} \approx 1$. The range of these two parameters are $0.5 \leq T_{LOW} \leq 1$ and $T_{LOW} < T_{HIGH} \leq 1$ because these thresholds are applied on $P_{Mitosis}$ which ranges between 0 and 1 since it is the average of two sigmoid functions. The final threshold, T_{SIZE} , will depend on the cell size.

Chapter 4

Intensity Based Algorithm

Studying of mitosis sequences such as Figure 4.1, shows that there is a drop in the intensity of the cell center during mitosis. This is caused by division of the nucleus and is a documented behavior in cancer tissue segments [27] and is observed to be true in embryo epithelia. Identification of these intensity drops forms the basis for an intensity approach for the detection of mitosis.

The intensity pattern needs to be studied relative to the embryo epithelia, not relative to the image coordinate system. That is, studying the intensity pattern of a pixel over time will not yield useful results as the embryo epithelia undergoes translations and deformation over time. In order to study the intensity pattern on the embryo epithelia, a reference frame that is fixed to the embryo epithelia and deforms along with the epithelia is needed (Section 4.1). This reference frame will be referred to as the material reference frame because it is relative to the material undergoing deformation. Once the material reference frame is identified, the intensity changes on the epithelia relative to the material reference frame can be obtained (Section 4.2). Thresholds can then be applied to these intensity changes to obtain the mitosis count and direction (Section 4.3). This entire process is outlined in Figure 4.2.

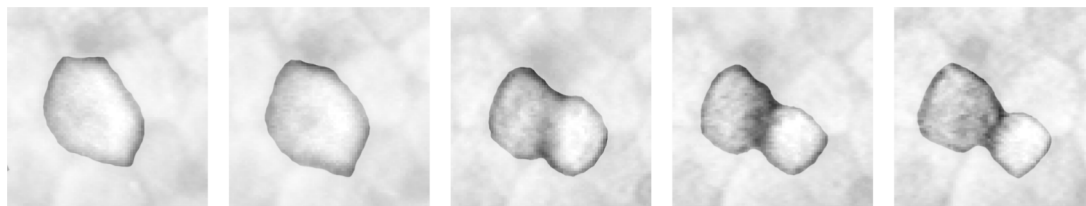


Figure 4.1: In this example of a single mitosis it can be clearly seen there is an intensity drop at the center of the cell during mitosis. This drop occurs during the division of the nucleus.

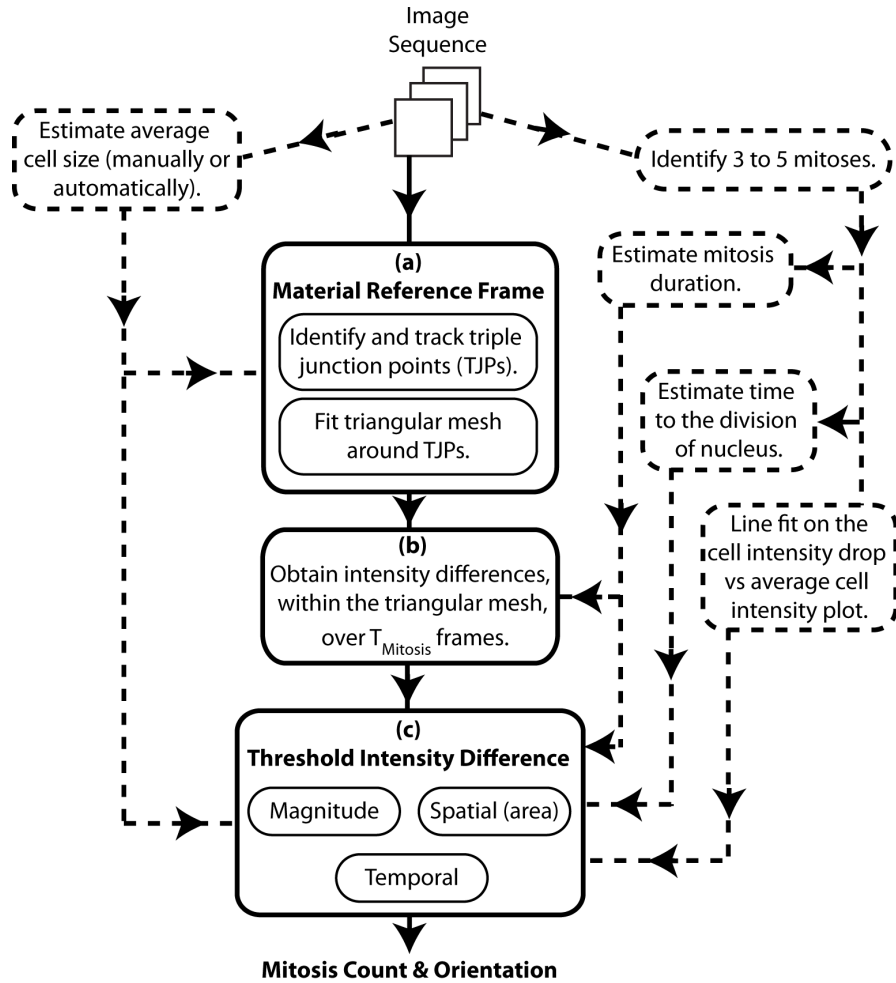


Figure 4.2: Overview of the intensity based algorithm. This algorithm detects mitosis by identifying intensity drops during the division of the nucleus. The dashed boxes represents parameters that are needed by the algorithm and must be estimated by the user. (a) A material reference that is fixed to the epithelia is obtained. (b) Relative to the material reference the intensity drops on the sections of the epithelium are identified. (c) Magnitude, area and temporal thresholds are applied on the intensity drops to obtain mitosis counts and orientation.

4.1 Material Reference Frame

In tracking non-rigid objects, such as the embryo epithelia, the object is typically represented using a triangular mesh [34, 35, 38, 39, 47]. Triangular meshes have also been used in registering images in medical image processing [17]. Here, the triangular mesh is used as the material reference frame. The triangular mesh will be deformed from one frame to the next using the real-time, non-rigid surface tracking algorithm presented in [34, 35]; this algorithm was chosen because it was simple to implement and unlike the other algorithms it used a regular triangular mesh on the first frame. The details of placing a triangular mesh on an image coordinate system are presented in Appendix B.

The triangular mesh (material reference frame) at frame t is represented by a set of L vertices $\mathbf{S}_t = \{v_1, \dots, v_L\}$. The goal of the triangular mesh deformation algorithm [35] is to obtain an estimate of these vertices on the next frame, $\hat{\mathbf{S}}_{t+1}$. This is accomplished using a set of key points, \mathbf{F}_t , that are tracked to the next frame, $\hat{\mathbf{F}}_{t+1}$, and a constraint on the amount of deformation that can occur. Mathematically the estimate $\hat{\mathbf{S}}_{t+1}$ can be obtained by minimizing the objective function [35]

$$\hat{\mathbf{S}}_{t+1} = \arg \min_{\mathbf{S}_{t+1}} \epsilon(\mathbf{S}_{t+1}) = \epsilon_D(\mathbf{S}_{t+1}) + \epsilon_C(\mathbf{S}_t, \mathbf{S}_{t+1}, \mathbf{F}_t, \hat{\mathbf{F}}_{t+1}). \quad (4.1)$$

Where $\epsilon_D()$ represents the mesh deformation constraint and $\epsilon_C()$ represents the correspondence between the tracked point sets \mathbf{F}_t and $\hat{\mathbf{F}}_{t+1}$ relative to the triangular mesh.

The deformation constraint $\epsilon_D()$ is modeled using a second order derivative constraint on the mesh vertices [19, 35]. This constraint models the embryo epithelia as a rubber sheet that is undergoing deformation; a similar constraint was used to track points on embryo epithelia [51]. The derivative constraint is formulated using a banded matrix \mathbf{K} as [35]

$$\epsilon_D(\mathbf{S}_{t+1}) = 0.5(\mathbf{X}^T \mathbf{K} \mathbf{X} + \mathbf{Y}^T \mathbf{K} \mathbf{Y}). \quad (4.2)$$

Refer to Appendix B.1 for details on deriving the \mathbf{K} matrix.

The correspondence constraint ϵ_C is [35]:

$$\epsilon_C(\mathbf{S}_t, \mathbf{S}_{t+1}, \mathbf{F}_t, \hat{\mathbf{F}}_{t+1}) = - \sum_{i=1}^L \rho(\|\hat{\mathbf{F}}_{t+1}(i) - T_S(\mathbf{F}_t(i), \mathbf{S}_t, \mathbf{S}_{t+1})\|, r). \quad (4.3)$$

$T_S()$ transforms the key points from frame t to frame $t + 1$ with respect to the triangular mesh using barycentric triplets [35]; discussion of the barycentric coordinate system is presented in Appendix B.2. The function $\rho(\delta, r)$ used in this work is slightly different from the one presented in [35] because in [35] for each feature point in frame t multiple feature points in frame $t + 1$ are detected. In this study

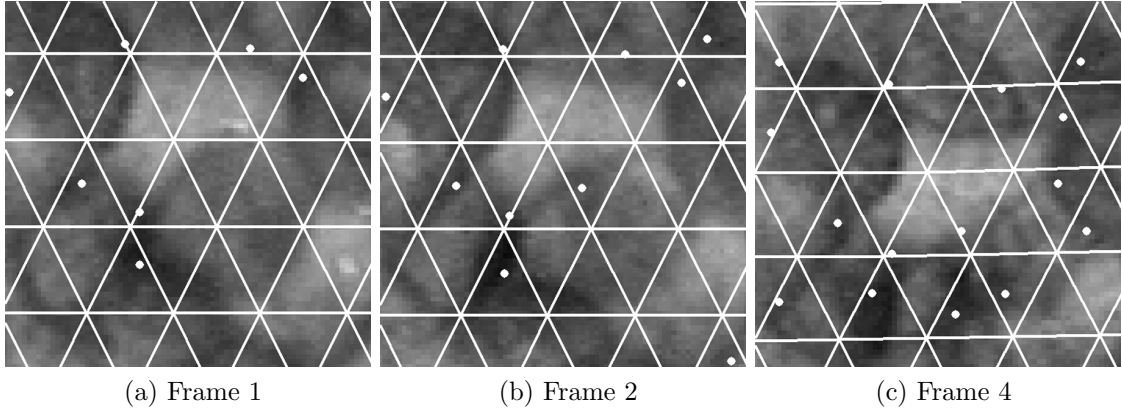


Figure 4.3: A regular triangular mesh from frame 1, represented by its vertices \mathbf{S}_t , is deformed to frame 2 using two constraints. The first constraint, smoothness constraint, minimizes the sum of all the second derivative along the mesh edges. The second constraint, correspondence constraint, attempts to keep the mesh fixed to a set of key points, \mathbf{F}_t , that are tracked from one frame to the next. The mesh is fixed to a key point by ensuring that the key point occupies the same location within a triangular grid, relative to the triangle’s vertices, from one frame to the next; this is accomplished using the barycentric coordinate system. The key points, \mathbf{F}_t , are illustrated in this figure as white dots. If a key point can not be tracked accurately to the next frame it is replaced by a new key point.

all points in \mathbf{F}_t have a one-to-one mapping with points in $\hat{\mathbf{F}}_{t+1}$ because they are tracked from one frame to the next. Thus,

$$\rho(\delta, r) = \frac{3(r^2 - \delta^2)}{4r^3} \quad (4.4)$$

where the value of r , as obtained from [35], starts as a large number and decreases after each iteration of the objective function (Eq. 4.1). The starting value for r was chosen as $3\Delta_{MAX}$ where Δ_{MAX} is the maximum possible displacement of a feature point between frame t and $t + 1$. This starting value of r is much smaller than the starting value recommended in [35] because very little deformation occurs between consecutive frames.

The material reference frame is always initialized as a regular triangular mesh, \mathbf{S}_t , on the first frame (Figure 4.3a). The key points, \mathbf{F}_t , are then selected on the first frame (white dots in Figure 4.3a) and tracked to the next frame (white dots in Figure 4.3b). The triangular mesh is then deformed from the first frame to the next using Eq. 4.1. In this way the triangular mesh is deformed from frame to frame till the N^{th} frame, (Figure 4.3c). Tracking and selection of these key points, \mathbf{F}_t , is explained in Section 4.1.1 and 4.1.2.

Figure 4.4 illustrates selected frames from the deformation of a triangular mesh on two epithelia surface. The first surface is a section of epithelia that is not on

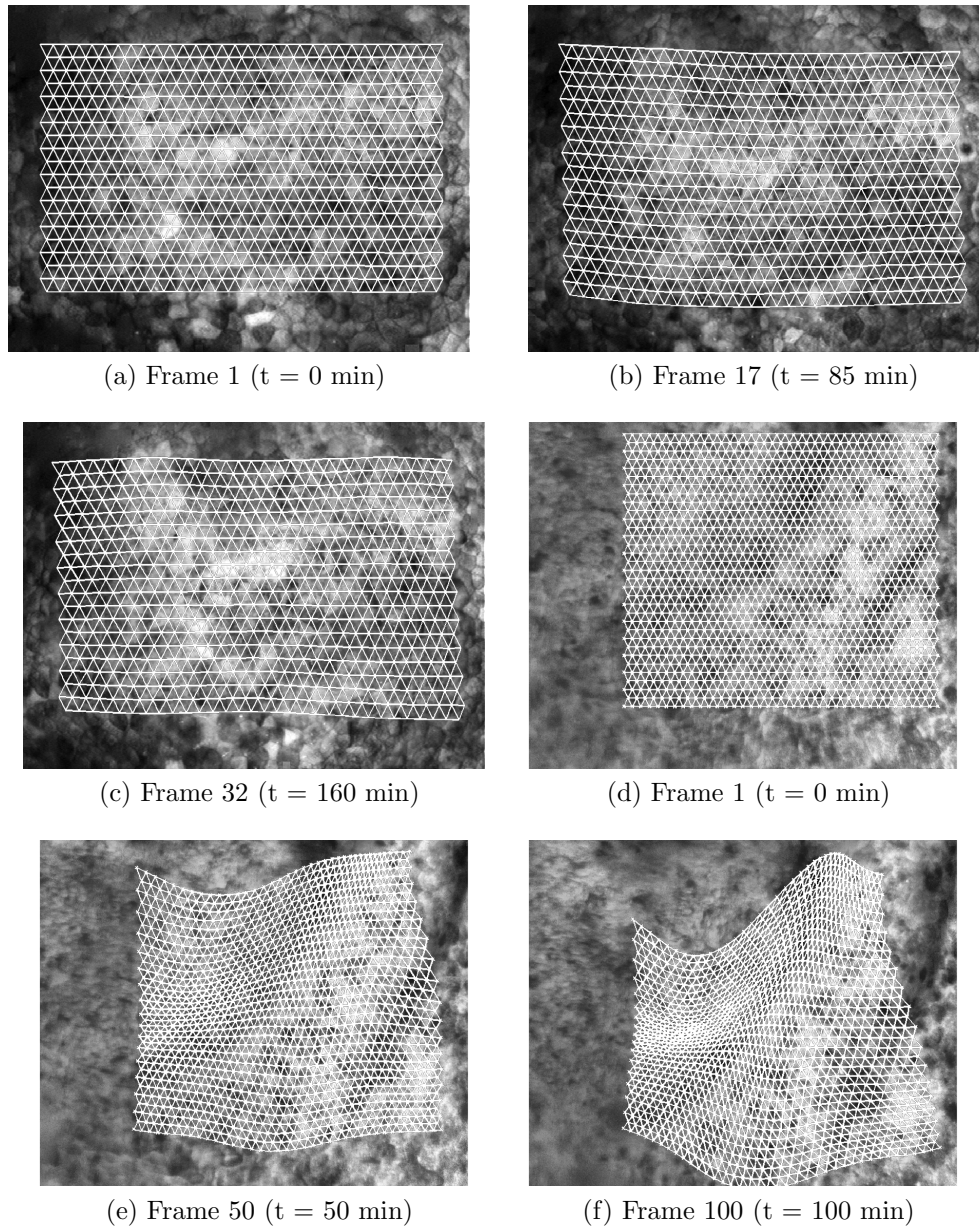


Figure 4.4: Triangular mesh attached to the embryo epithelia; to be used as a material reference frame. (a-c) Early stage embryo development. (d-f) Late stage embryo development at the neural ridge area.

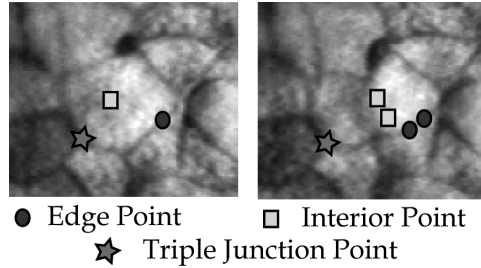


Figure 4.5: Illustration of the aperture problem. When matching points using local region of interest only the triple junction points can be uniquely matched from frame to frame; boundary and cell center points can be matched to multiple locations on the next frame.

the neural ridge or neural plate; most of the surface of the epithelia is similar to this tissue segment. The second surface is a section of epithelia on the neural ridge. As illustrated in this figure, the rubber sheet model conforms well to the non-neural ridge areas, however, on the neural ridge there is a fold in the tissue which contradicts the second derivative smoothness constraint. If the location of the neural ridge fold is known, a fold constraint can be introduced on the nearby grid vertices. In this study the location of the neural ridge is not known. As a result, images of epithelia along the neural ridge or neural plate are not used.

4.1.1 Key Point Identification and Tracking

The points F_t are tracked using the Kalman Filter with the phase disparity measure as discussed in Section 2.3. For the phase disparity measure a Gabor filter bank with twelve filters are used. The filters were tuned for bandwidths of 0.5, 1 and 1.5 times the cell boundary; this accounted for any deviations of the cell boundary width from the average boundary size obtained from the user. For each of the three filter bandwidths, orientations of $-45^\circ, 0^\circ, 45^\circ$ and 90° are used. The tuning of Gabor filters to the specified parameters is illustrated in [46].

The orientations of 0° and 90° are used to account for all highly horizontal and vertical cell boundaries and the orientations of -45° and 45° account for diagonal cell boundaries. Ideally, to account for cell boundaries at all angles and larger deviations from the average cell boundary, it would be beneficial to tune filters at much finer resolution in bandwidth, $0.1 : 0.1 : 1.9$ times the line width, as well as orientation $-90^\circ : 1^\circ : 90^\circ$. However, this will result in a much larger number of filters and significantly increase the computational cost.

The points to be tracked need to be chosen such that they can be uniquely matched between frames. To isolate these points, all points on the cell sheet are classified as either lying inside a cell, on a boundary between two cells or on a junction between multiple cells. From Figure 4.5, it can be seen that points on the cell boundary and cell center can not be uniquely matched from one frame to the

next using a local region of interest because multiple nearby points have the same intensity pattern. This problem is called the *aperture problem* and it occurs in all local region based tracking schemes [44]. As a result of the aperture problem, only triple junction points (TJPs) are selected as suitable points for tracking.

The key points \mathbf{F}_t are selected as TJPs on the first frame of the epithelia image sequence. If a point being tracked is lost, then it is replaced by a new TJP from the current frame. A tracked point $\hat{\mathbf{F}}_t(i)$ is said to be lost if it is no longer close to a TJP. The weight of a tracked point $\hat{\mathbf{F}}_t(i)$ being closed to TJP is defined as

$$P(i) = \exp\left(\frac{\left[\min\left(\|\hat{\mathbf{F}}_t(i) - \underline{a}\|\right)\right]^2}{-2\sigma^2}\right), \forall \underline{a} \in \mathbf{A}_t. \quad (4.5)$$

\mathbf{A}_t is the list of all TJPs on frame t and σ controls the allowable variability of the distance between a tracked point and the closest TJP. The value of σ must be smaller than the maximum movement expected between two frames. In this study σ was chosen as the width of the cell boundaries. To account for focus and illumination changes, a threshold of $P_{Thresh} = 0.5$ is applied on the average of $P(i)$ over the last $N = 4$ frames.

4.1.2 Triple Junction Point Detection

The TJPs, \mathbf{A}_t , can be detected by finding intersections of cell boundaries. To isolate all TJPs, all cell boundaries need to be found such that each individual cell is segmented in the image; this is not possible due to poor contrast of cell boundaries as stated before in Section 2.1. Therefore, the TJP detection algorithm presented here will not detect all TJPs.

To detect cell boundaries the Gabor filter (GF) is used. The use of the GF to detect cell boundaries was successfully demonstrated in electron microscopy images [46]. Four GFs, as formulated in [46], are used to detect cell boundaries. All four filters are tuned to the width of the cell boundaries and assumed to have a line length of two times the width; converting line width and length to the frequency and bandwidth of the GF is presented in [46]. The four filters have orientations of $-45^\circ, 0^\circ, 45^\circ$ and 90° .

The magnitude of the real part of the Gabor filtered images can be combined to determine the magnitude of the cell boundaries. The four filtered images \mathbf{I}_{-45}^{RGF} , \mathbf{I}_0^{RGF} , \mathbf{I}_{45}^{RGF} and \mathbf{I}_{90}^{RGF} are first combined in pairs to obtain two estimates of the edge magnitude. The first estimate $\hat{\mathbf{B}}_1$ is obtained in Eq. 4.6 using the 0° and 90° orientation filters. These two orientations of the GF will give high responses for horizontal and vertical boundaries but weaker responses for diagonal boundaries as illustrated in Figure 4.6b. The second estimate $\hat{\mathbf{B}}_2$ is obtained in Eq. 4.7 using the -45° and 45° orientation filters. These two orientations of the GF will give high responses for diagonal boundaries and weaker responses for horizontal and

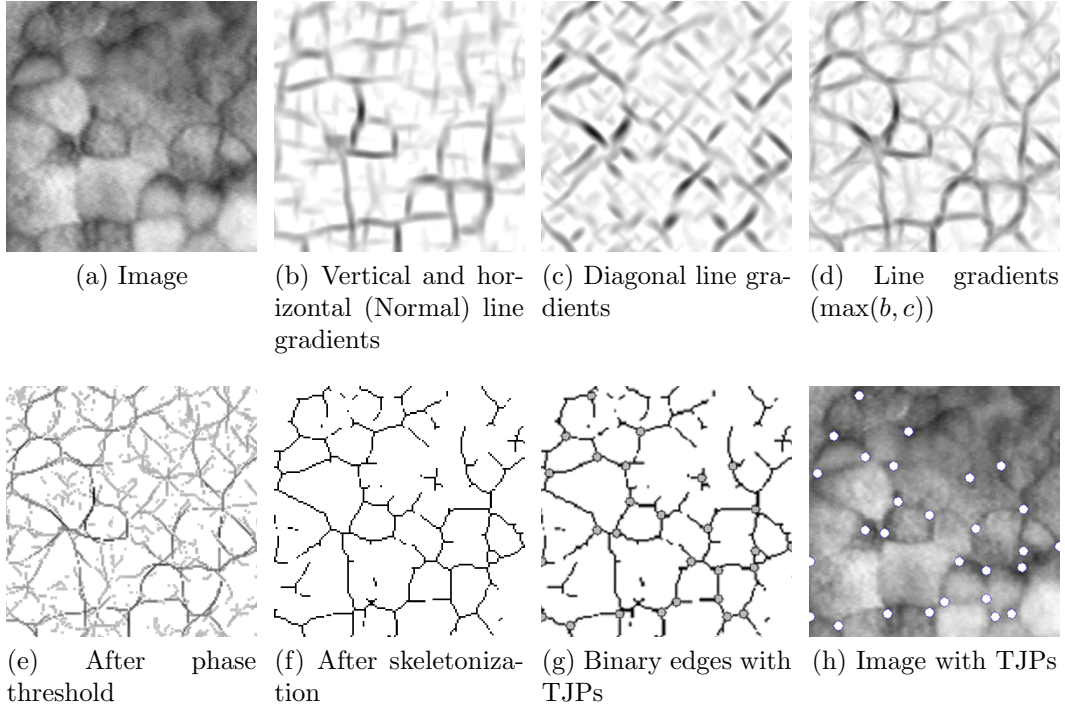


Figure 4.6: Illustrates the steps in determining triple junction points (TJPs). Normal and diagonal line gradients are obtained using the magnitude response of normal and diagonal real Gabor filters respectively. Maxima of normal and diagonal line gradients are obtained as the cell boundary gradient. The Gabor filter phase is used to threshold the line gradient. Skeletonization is used to thin binary lines to one pixel wide. Finally TJPs are detected on the binary line image. Note the gradient images have been scaled for better display.

vertical boundaries as illustrated in Figure 4.6c. The two boundary estimates are then combined in Eq. 4.8 to obtain a more accurate estimation of cell boundary strengths in all orientations (Figure 4.6d).

$$\hat{\mathbf{B}}_1 = \sqrt{(\mathbf{I}_0^{RGF})^2 + (\mathbf{I}_{90}^{RGF})^2} \quad (4.6)$$

$$\hat{\mathbf{B}}_2 = \sqrt{(\mathbf{I}_{-45}^{RGF})^2 + (\mathbf{I}_{45}^{RGF})^2} \quad (4.7)$$

$$\mathbf{B} = \max(\hat{\mathbf{B}}_1, \hat{\mathbf{B}}_2) \quad (4.8)$$

When applying the complex GF to an image, the magnitude of the imaginary response (\mathbf{I}^{IGF}) is the smoothed first spatial derivative and the magnitude of the real response (\mathbf{I}^{RGF}) is the smoothed second spatial derivative, where the orientation and smoothness of the derivatives corresponds to the GF orientation and bandwidth. Based on this behavior the central pixel of a line will have an imaginary response of zero and an absolute real response of a large number (Figure 4.7).

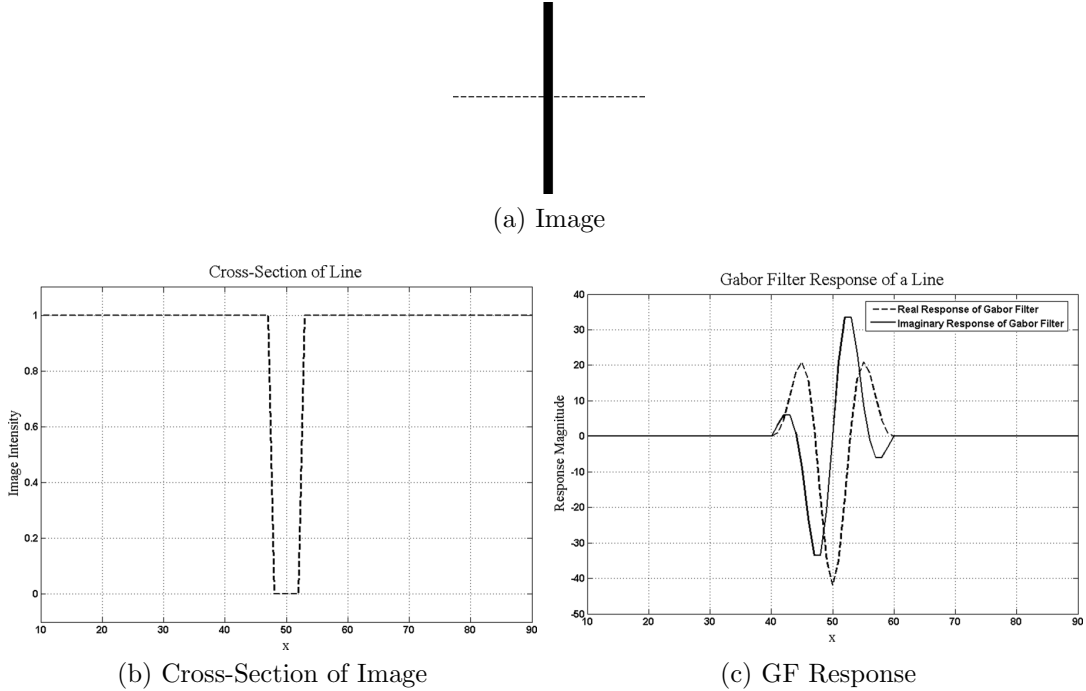


Figure 4.7: (a) Image of a line. The dotted line represents the location of the cross-section studied in (b-c). (b) The intensity profile along the cross-section of the image. (c) The real and imaginary response of a Gabor Filter (GF) tuned to the line width and orientation. The phase of the GF at the center of the line ($x = 50$) is $\arctan(I^{IGF})/(I^{RGF}) = \arctan 0/(-42) = 180^\circ$.

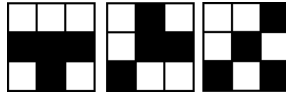


Figure 4.8: Masks used to find initial estimates of triple junction points.

The phase response of a GF, $\arctan(I^{IGF})/(I^{RGF})$, at the central point on the line will be $\arctan 0/x = 180^\circ$ where $|x| \gg 0$. Therefore, erroneous boundaries in \mathbf{B} can be eliminated by thresholding the phase response of the GF (Figure 4.6e).

The lower and upper thresholds placed on the phase response are 170° and 190° . A range of phase are accepted because due to discretization the imaginary response magnitude of the GF (first spatial derivative) at a pixel is sometimes small but not zero. Once the phase threshold has been accomplished, the potential boundaries are then thresholded to a binary image and thinned to one pixel width using a morphological skeletonization operation [14]. The resulting binary boundary image (Figure 4.6f) is then used to obtain TJPs.

Given the binary boundary image, there are several methods available for detecting TJPs [28, 32, 45]. In this work a very simple algorithm is used, instead of the ones presented in [28, 32, 45] because the methods presented in [28, 32, 45] are complicated by the need for obtaining the angles between the three branches

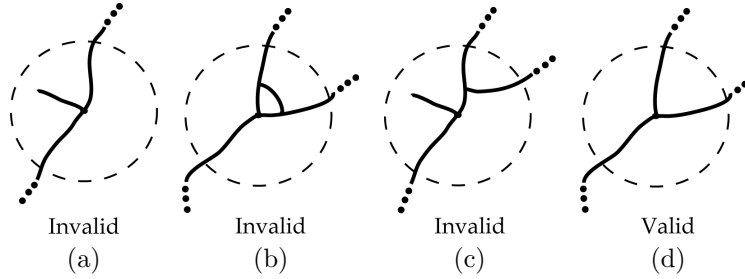


Figure 4.9: Invalid and valid triple junction points (TJPs) based on the branch length test using a circle. (a) Only two branches from TJP are longer than circle radius. (b-c) Within the circle the branches meet at a point other than the TJP (center of circle). (d) Valid TJP is one that has three branches with length greater than the radius of circle and the three branches only meet at the TJP.

meeting at the TJPs. The method used here starts off by obtaining initial estimates of TJPs by filtering the binary boundary image using all four 90° rotations for each of the three masks shown in Figure 4.8. These initial estimates are then improved by checking the lengths of each of the three branches meeting at the TJP. This assumes that true TJPs will have long branches and TJPs caused by noise will not.

To check the length of the branches, a circle of radius R is placed on each of the potential TJPs. The point is kept as a TJP if the three branches from the point reach the circumference of the circle without touching each other. Figure 4.9 illustrates some valid and invalid TJPs. Of the detected TJPs, all points that are Δ_{MAX} distance apart from each other are added to A_t , Figure 4.6g.

4.2 Intensity Analysis on Material Reference Frame

The material reference frame (triangular mesh, S_t) can be thought of as a Lagrangian reference frame for the embryonic epithelium. That is, the epithelia within each triangular grid over time is the same tissue. Having obtained this material reference frame, the intensity behavior over time of each triangular section of epithelia can be studied to determine locations where there is a drop in intensity. As stated before, these drops in intensity are potential locations of mitosis.

The intensity of each triangular epithelia section is represented by $G_t(i)$, the average intensity of all image pixels within the triangular grid; refer to Appendix B for details. The intensity change in the epithelia section, $D_t(i)$, is then obtained as the difference in the average intensity of the triangular grids:

$$D_t(i) = G_t(i) - \min(G_{t+1}(i), G_{t+2}(i), \dots, G_{t+t_{Mitosis}}(i)). \quad (4.9)$$

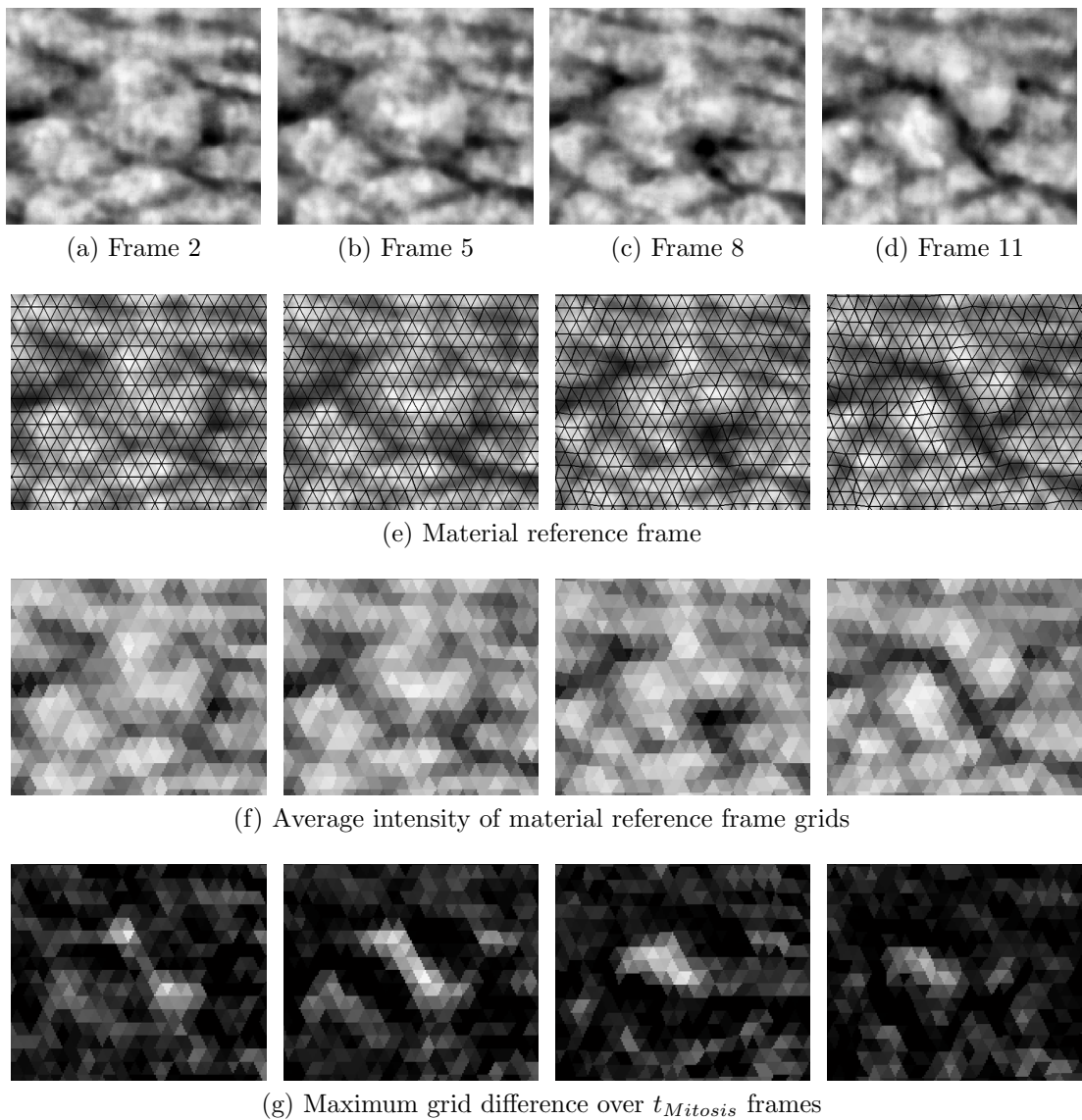


Figure 4.10: Continued To Next Page.



(h) Frame difference after linear magnitude threshold



(i) Frame difference after size threshold



(j) Frame difference after temporal threshold

Figure 4.10: An example processing of an image sequence using the intensity based mitosis detection algorithm presented in this thesis. (a-d) Select frames from a time-lapse image set with one true mitosis at the center of the frames. (e) The material reference frame at each frame obtained by deforming triangular mesh. (f) The average intensity of each grid in the material reference frame. (g) Maximum frame difference over $t_{Mitosis}$ frames. (h) Frame difference after magnitude thresholds T_m and T_b . (i) Frame difference after size threshold T_{SIZE} on 12-connected objects in the triangular mesh (material reference frame). (j) Frame difference after temporal threshold $t_{Mitosis} - t_{NucleusDiv} + 1$.

The value of $t_{Mitosis}$ is chosen by the user such that it represents the duration of mitosis in frames. All negative values of $D_t(i)$ are set to zero because only decreases in intensity are of interest. These drops in intensity values are then used to determine if each triangular section of epithelia is on a cell undergoing mitosis. This approach is only valid if there are now sudden changes in the global illumination within the $t_{Mitosis}$ frames.

An example of the grid average intensity, G_t , and the frame difference, D_t , are illustrated in Figures 4.10f and 4.10g respectively. The actual frames and material reference frame used to obtain these average intensity and frame difference are presented in Figures 4.10a to 4.10e.

4.3 Mitosis Count and Orientation

Several criteria can be used to threshold D_t and obtain the location of mitosis. First, since mitosis tends to have a large decrease in intensity, a magnitude threshold can be applied. Secondly, if the triangles in the mesh are smaller than the cell size, then mitosis locations will have several adjacent triangular grids with large intensity changes allowing for a spatial spread (area) threshold. Finally, since mitosis occurs over several frames, the areas of large intensity change will persist over multiple frames allowing for a temporal threshold.

The linear magnitude threshold modeled applied to D_t to obtain D'_t is defined as

$$D'_t(i) = \begin{cases} 1 & D_t(i) > G_t(i)T_m + T_b \\ 0 & \text{Otherwise.} \end{cases} \quad (4.10)$$

The threshold is based on the original average intensity of each grid, $G_t(i)$, because bright cells were observed to have a larger decrease in intensity during mitosis than a darker cell. The values of T_m , the slope of linear threshold, and T_b , y-intercept of linear threshold, are highly dependent on the quality of the image.

Currently the values of T_b and T_m are selected by plotting the intensity drop vs average cell intensity of several mitoses; typically 2 to 5 hand-identified mitoses are used for this purpose. The number of hand-identified mitoses used depends directly on the variation of cell intensities in the image sequence; larger the cell intensity variation, the larger the number hand-identified mitoses needed. Once the intensity drop vs average cell intensity of manually detected mitoses are plotted, a least squares fit of a line through these points will yield the slope (T_m) and y-intercept (T_b) is chosen as a value slightly smaller than the y-intercept obtained from the least squares fit. This is illustrated in Figure 4.11. The slope T_m will be shallow, nearly horizontal, if all the cells in the images have relatively the same intensity values and will be steep if the image contains both dark and light cells. Finally if T_b is negative then all cells with intensity from 0 to the x-intercept will be ignored

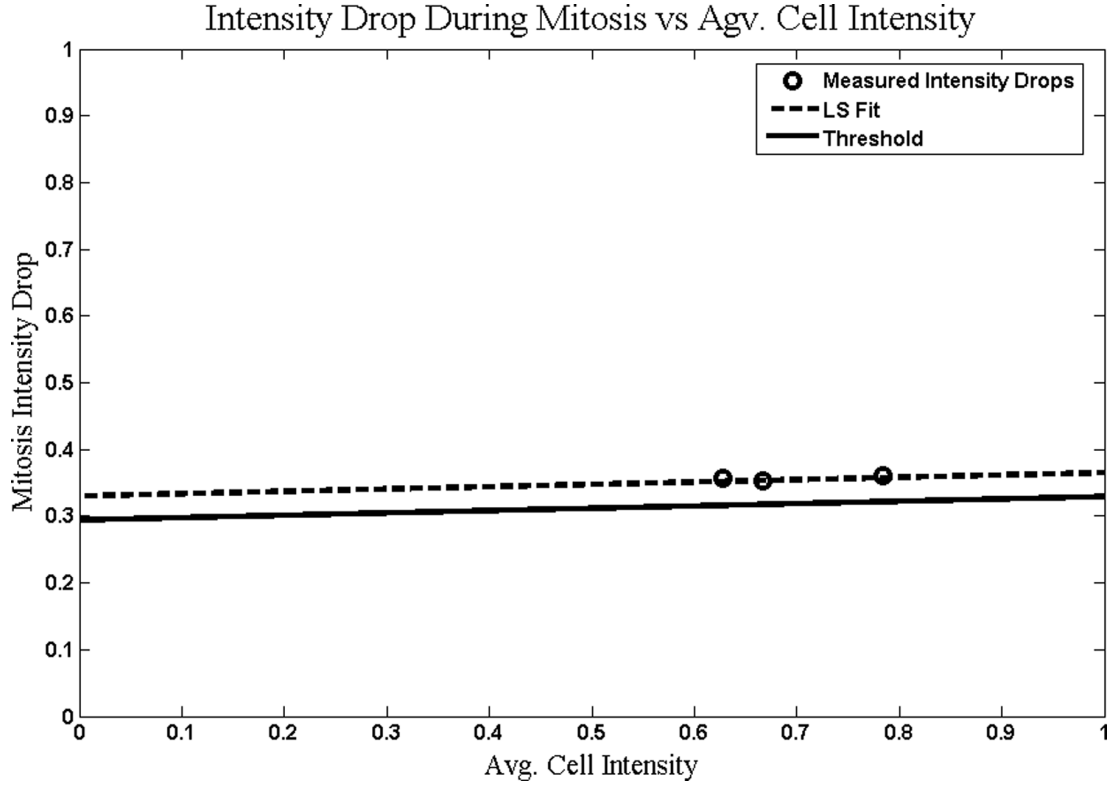


Figure 4.11: The procedure for selecting the intensity drop threshold as a function of average cell intensity. First plot the intensity drop during mitosis vs average cell intensity points for some known measured mitoses (plotted as o). Then using the least squares algorithm fit a line through these points (dashed lines). The intensity drop threshold then has the same slope as the least squares fit but the y-intercept will be slightly smaller than the least squares y-intercept.

when detecting mitosis. The sensitivity of algorithm performance to the choice of T_b and T_m is presented in Section 5.2.

The result of magnitude threshold, D'_t , is a set of 12-connected object on the triangular mesh (Figure 4.10h). The 12-connected objects were chosen because on a triangular grid (material reference frame) 12-connectivity is equivalent to 8-connectivity typically used on the rectangular grid image coordinate systems. Refer to Appendix B for details on 12-connectivity. The area of each 12-connected object, in number of triangles, is calculated and thresholded to obtain D''_t (Figure 4.10i), a more refined estimates of mitosis locations.

$$D''_t(\mathbf{P}_i) = \begin{cases} 1 & \text{if } size(\mathbf{P}_i) > T_{SIZE} \\ 0 & \text{Otherwise.} \end{cases} \quad (4.11)$$

where \mathbf{P}_i is a list of all triangles in the i^{th} 12-connected object in D'_t . The threshold T_{SIZE} is chosen as the number of triangles that can fit within the width of the

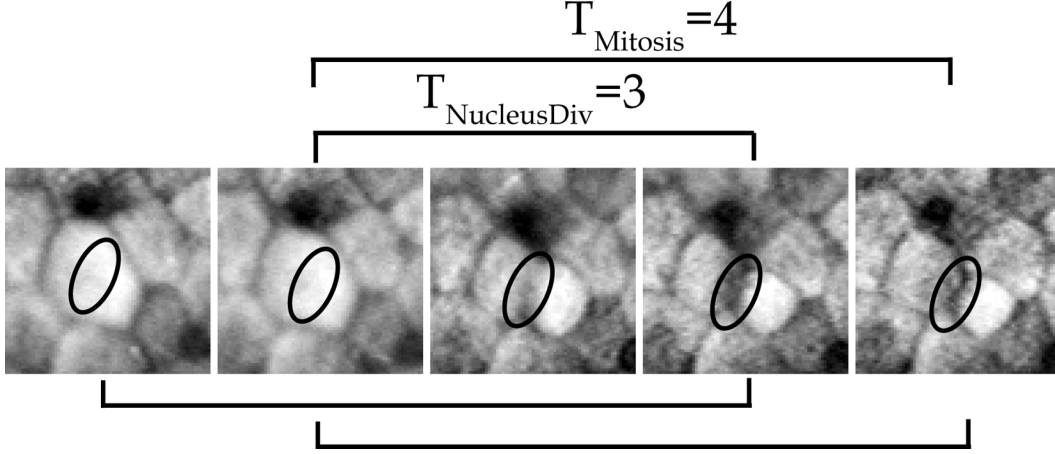


Figure 4.12: The time for mitosis and nucleus division is illustrated. The maximum decrease in intensity is seen in two frames ($t_{Mitosis} - t_{NucleusDiv} + 1 = 4 - 3 + 1 = 2$). The bottom braces show the two instances when a large intensity drop will be seen because these two set of $t_{Mitosis}$ frames contain the cell before start of mitosis and during nucleus division. The elliptical region marked on each frame indicates the region of the cell that undergo the intensity drop due to nucleus division.

average cell; the width of the average cell can be provided by the user manually or obtained automatically [25].

Finally, the remaining 12-connected objects in D'_t are further pruned using the temporal spread. Given $t_{Mitosis}$, the duration of mitosis and $t_{NucleusDiv}$ the time to the nucleus division (Figure 4.12), the temporal spread of the intensity drops can be estimated as $t_{Mitosis} - t_{NucleusDiv} + 1$ frames. As a result, any object in D'_t that is not present for $t_{Mitosis} - t_{NucleusDiv} + 1$ frames are deleted as a false positive (Figure 4.10j). An object in frame t is said to be present in frame $t + 1$ if there is a 12-connected object in frame $t + 1$ that spatially overlaps it.

When using triangular mesh representation for the embryo epithelia, the triangular mesh will have a lower resolution than the image because the mesh is placed on top of the image. To ensure that the cells are still distinguishable, the resolution of the triangular mesh must be higher than the resolution of the cells. However, tracking a high resolution triangular mesh from frame to frame is computationally expensive. Therefore, a low resolution mesh can be used for tracking and then later interpolated to obtain a resolution higher than the cell resolution. Interpolating the low resolution mesh works well so long as the starting low resolution mesh is slightly smaller than the cell resolution.

Each detected mitosis consists of a set of connected triangles on several consecutive frames. The union of these triangles, as illustrated in Figure 4.13, are obtained in list H ; where the list H contains the centroid of each triangle, $H(i) = \underline{c} = (x, y) =$ centroid of triangle i . The maximum intensity difference of each of the triangles in H are obtained in list I . Given H and I the weighted mean and covariance of the spread of the triangle centroid can be obtained as:

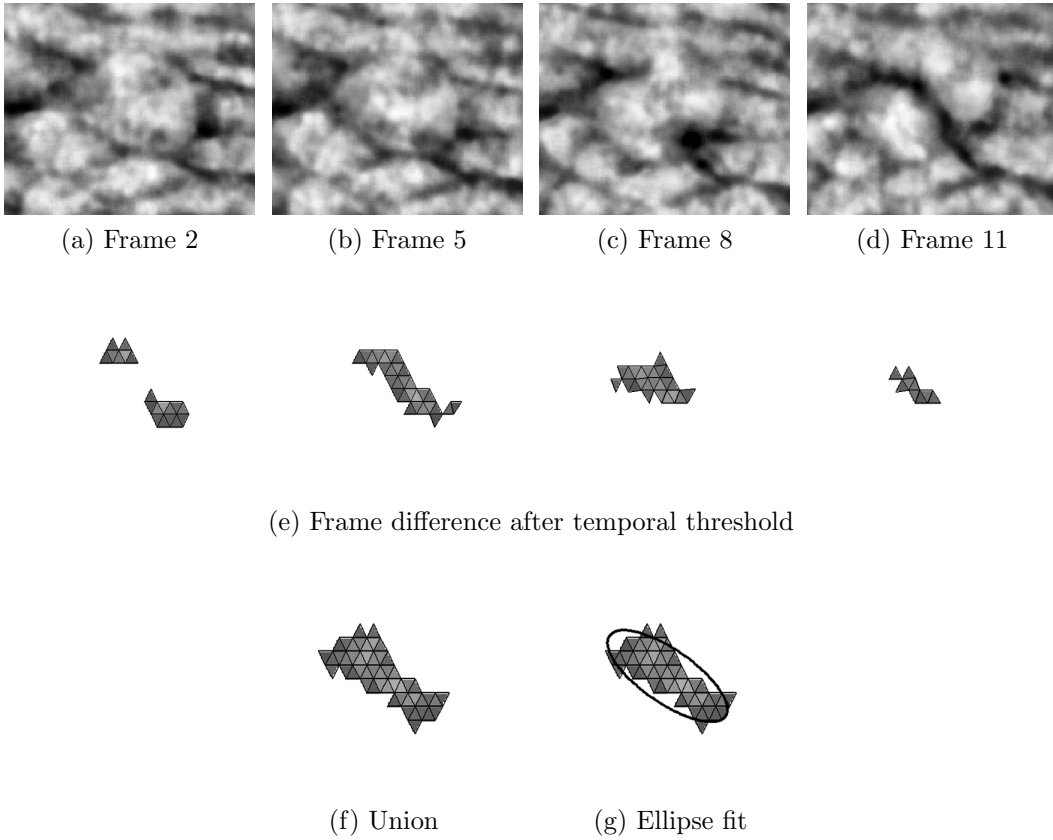


Figure 4.13: Given the intensity difference at all triangles in the material reference frame that have met all the threshold conditions (e), the union of these frames consists of all spatially overlapping connected components over consecutive frames (f). Using the maximum difference and the centroid of the triangles in the union (f) an ellipse can be fit around these intensity differences. The minor axis of the ellipse will be the orientation of the mitosis.

$$\bar{h} = \frac{\sum_i \mathbf{H}(i) \mathbf{I}(i)}{\sum_i \mathbf{I}(i)} \quad (4.12)$$

$$\mathbf{S} = \frac{1}{\sum_i \mathbf{I}(i)} \begin{bmatrix} \sum_i \mathbf{I}(i) (\mathbf{H}(i)_x - \bar{h}_x)^2 & \sum_i \mathbf{I}(i) (\mathbf{H}(i)_x - \bar{h}_x) (\mathbf{H}(i)_y - \bar{h}_y) \\ \sum_i \mathbf{I}(i) (\mathbf{H}(i)_x - \bar{h}_x) (\mathbf{H}(i)_y - \bar{h}_y) & \sum_i \mathbf{I}(i) (\mathbf{H}(i)_y - \bar{h}_y)^2 \end{bmatrix} \quad (4.13)$$

The direction of the mitosis is then obtained as the direction of the eigenvector of \mathbf{S} with the smallest eigenvalue. Essentially the union of the triangles should lie in a line along the width of the cell, such that when an ellipse is fit around these triangles the major axis will be along the width of the cell and the minor axis should represent the direction of the two daughter cells.

Chapter 5

Algorithm Performance

The algorithms were tested on several time-lapse image sequences from two embryos. The first embryo was at an early stage of development (stage 9 [1]); approximately 23 hours into embryogenesis. The second embryo was at a later stage of development (stage 12 [1]); approximately 45 hours into embryogenesis. The frequency of mitoses was observed to be high at the early stage embryo development and very low during later stage development. As a result of this, manual ground truth detection on early stage embryo images are easier than later stage embryo images.

The testing data used are outlined in Table 5.1. One image sequence from an early stage embryo and fourteen image sequences from the same late stage embryo are used. The number of mitoses and orientation within each image sequence was manually determined. The parameters of an ellipse, that modeled the average cell in the image sequence, were obtained using the algorithm presented in [25]. High-magnification images of the early stage embryo development were not available for use in this study because of the unavailability of young embryos. The late stage images used a much higher magnification as seen by the cell resolution.

Before proceeding with the algorithm analysis, a discussion on the method for evaluating these mitosis detection algorithms is needed. Mitosis detection, as presented in this work, is not a classification problem, it is an event detection problem. As an event detection algorithm, the only information available are the number of correctly detected mitoses (TP - true positive), the number of incorrectly detected mitoses (FP - false positive) and the number of mitoses not detected (FN - false negative). If this was a classification problem then the number of cells correctly classified as not undergoing mitosis (TN - true negative) would also be known. However, since the total number of cells on the images are not known the TN count is not known.

Event detection algorithms can be analyzed using precision (P) [30]

$$P = \frac{TP}{TP + FP} \tag{5.1}$$

Table 5.1: Test Data Sets

Set	Sequence #	# of Frames	Frame Intervals (min)	Avg. Cell Model in Pixels			# of Mitoses
				Area	Major Axis	Minor Axis	
Early Stage	1	25	5	317	21.8	18.5	94
Late Stage	2	21	1	2567	76.2	42.9	1
	3	51	1				2
	4	21	1				1
	5	21	1				1
	6	21	1				1
	7	21	1				1
	8	21	1				1
	9	21	1				2
	10	21	1				2
	11	21	1				1
	12	21	1				3
	13	21	1				2
	14	21	1				1
	15	61	1				5

and recall (R) [30]

$$R = \frac{TP}{TP + FN}. \quad (5.2)$$

Precision, P , is the fraction of mitoses correctly detected by the algorithm out of all the locations detected as mitosis by the algorithm. Recall, R , also called the true positive rate, is the fraction of mitosis correctly detected by the algorithm out of the total mitosis present in the test data set. Ideally a precision of 100% and a recall of 100% is desired by all detection algorithms.

The performance rate or score for a given algorithm can be given by the F -measure, F_β , [30]:

$$F_\beta = \frac{(\beta^2 + 1)PR}{\beta^2 P + R}. \quad (5.3)$$

The parameter β controls the importance of recall over precision. In this study both precision and recall are assumed to be equally important thus $\beta = 1$.

Finally the performance of an algorithm relative to a parameter in that algorithm can be studied using the precision-recall curve (PRC). The PRC is related to the receiver operator curve (ROC) [13] which is used to study classification algorithms. The plots of the PRC used in this study follow the interpolation method presented in [13].

Table 5.2: Motion Algorithm Parameters

Set	k_{VelMag}	b_{VelMag}	Optimal		
			T_{SIZE}	T_{HIGH}	T_{LOW}
Early Stage	1	5	200	0.65	0.5
Late Stage	1	7	400	0.95	0.5

Table 5.3: Search Range Used to Obtain the Optimal Thresholds for Motion Algorithm

Set	Search Range		
	T_{SIZE}	T_{HIGH}	T_{LOW}
Early Stage	50 : 50 : 300	$T_{LOW} : 0.05 : 1$	0.5 : 0.05 : 1
Late Stage	100 : 50 : 500	$T_{LOW} : 0.05 : 1$	0.5 : 0.05 : 1

5.1 Motion Based Algorithm

For the motion based algorithm the main parameters selected by the user are k_{VelMag} and b_{VelMag} from Eq. 3.6 and the thresholds T_{LOW} , T_{HIGH} and T_{SIZE} as discussed in Section 3.4. The values of k_{VelMag} and b_{VelMag} are chosen based on the data and are presented in Table 5.2. These parameters, presented in Table 5.2, were chosen using 3 of the 94 manually detected mitoses on the early stage image set and using image sequence 2 and 3 for the late stage image set; these mitoses were not used in the testing phase. Only a loose guideline was given in Section 3.4 for choosing the thresholds T_{LOW} , T_{HIGH} and T_{SIZE} , as a result the optimal threshold triplet (T_{LOW} , T_{HIGH} , T_{SIZE}) was found as the triplet that maximized the F -measure, $F_{\beta=1}$. The optimal threshold triplet is given in Table 5.2 and the range of the threshold triplets searched to obtain the optimal triplet is given in Table 5.3. Based on the optimal threshold values, T_{LOW} is in fact 0.5 as expected for both the early and late stage image sets. The value of T_{HIGH} is close to 1 for the late stage set but not for the early stage set. The low value of T_{HIGH} would suggest that the values of $P_{Mitosis}$ for the early stage do not span the entire range of 0 to 1.

Given the parameters in Table 5.2, the confusion matrices for mitosis detection by the motion based algorithm are presented in Figure 5.1. Based on the confusion matrices, the algorithm performance is determined using the F -Measure as 68.2% for the early stage image set and 66.7% for the late stage image set. Based on the F -Measure the performance of this algorithm is better than a random guess and since no other algorithms exists this is a definite progress. However based on the personal from the Embryo Biomechanics lab a performance of 80% or higher is needed before the algorithm can be used for studying embryo development.

The performance of this algorithm on the two image sets are similar, but the cause of the low performance for the two image sets are widely different. To see the difference, the precision-recall points for all threshold triplets (T_{LOW} , T_{HIGH} ,

		Predicted				Predicted	
		Positive	Negative			Positive	Negative
Act- ual	Positive	58	33	Act- ual	Positive	16	5
	Negative	21	N/A		Negative	11	N/A

(a) Early stage

(b) Late stage

Figure 5.1: The confusion matrices for the motion based mitosis detection algorithms on the early and late stage image sets using the optimal threshold values as determined by maximizing the F -Measure.

T_{SIZE}) in the range given in Table 5.3 are plotted in Figure 5.2. From the precision-recall point plot, for the early stage image set high precision rates are achieved but high recall rates are not achieved. In the late stage image set it is the opposite, that is high recall rates are achieved but high precision rates are not achieved. This means that for the early stage image set FN are common and for the late stage image set FP are common.

FNs are caused when the *mitosis motion field prototype* is not detected at an actual mitosis location. This occurs when the local motion field, where the *mitosis motion field prototype* appears, is altered by some other type of motion. As discussed in Section 3.2, the image motion field is composed of a global translation \vec{T} , local image motion \mathcal{L} and large scale reshaping \mathcal{R} . Since for high-magnification images the global translation \vec{T} dominates the large scale reshaping \mathcal{R} , the reshaping term \mathcal{R} was ignored. The high FN rate in the early stage image set suggests the presence of the large scale reshaping, \mathcal{R} . This indicates that the level of magnification used for the early stage image set was not high enough to counter act the large scale reshaping. For the late stage image set, a higher magnification level is used which resulted in the absence of large scale reshaping causing the lower FN rate.

FPs are caused when the *mitosis motion field prototype* is detected at locations where mitoses are not present. As with the FNs, FPs occurs due to a poor estimation of local motion field. In the case of FPs the poor local motion field is a result of illumination changes. The late stage image set has a larger intensity change between frames than the early stage image set. Furthermore the late stage image set also has higher noise levels due to the high magnification used. These intensity changes and noise levels are detected by the optical flow algorithm, used to estimate local image motion, as actual epithelia motion. These false motions has increased the FP rate of mitosis detection in the late stage image set.

The error in the mitosis orientation for all detected mitoses in the early and late stage image sets are illustrated in Figure 5.3. The figure shows that the error rates are quite high for the orientation. Accuracy is marginally affected by the discrete 5° rotations of the *mitosis motion field prototype* that are used. The main component that affects the accuracy is how well the mitosis motion field matches the *mitosis motion field prototype*. Studying the mitosis with low orientation error it can be

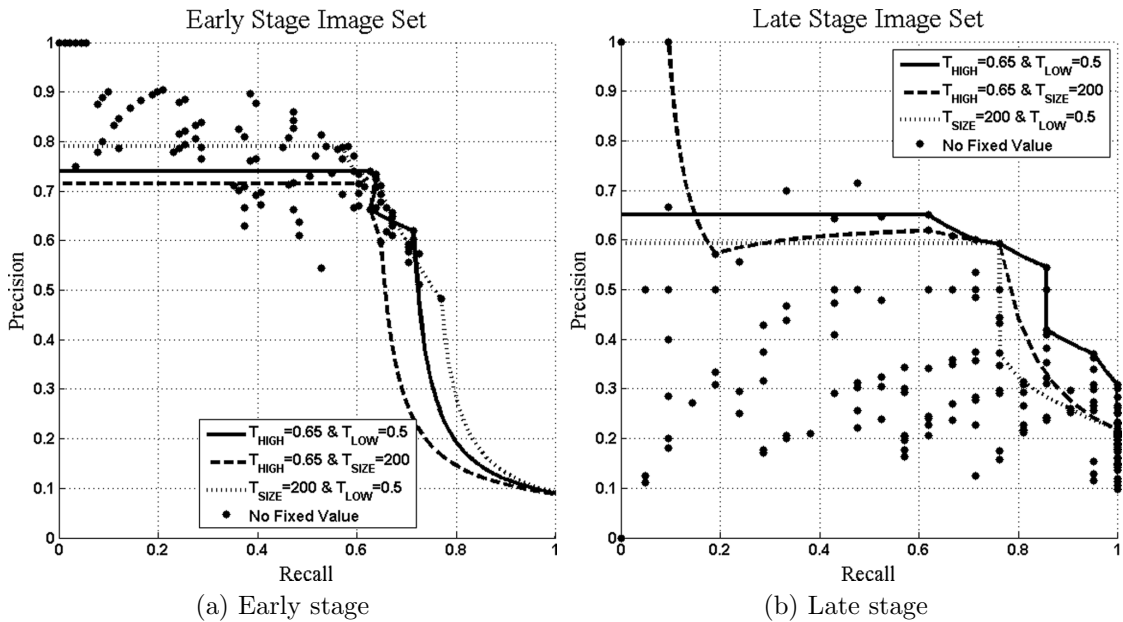


Figure 5.2: The precision-recall points for the motion based algorithm as function of $(T_{LOW}, T_{HIGH}, T_{SIZE})$ are presented for the early and late stage image set. The PRC are obtained by fixing two of the thresholds to the optimal value based on F -Measure. Large scale reshaping motion is present in the early stage image set due to the use of low-magnification images; this resulted in high FN rate. The late stage image set uses high-magnification images thus FN rate are lower than the early stage image set. However, due to the high magnification, there are illumination changes and noise present in the late stage image set; this resulted in high FP rate.

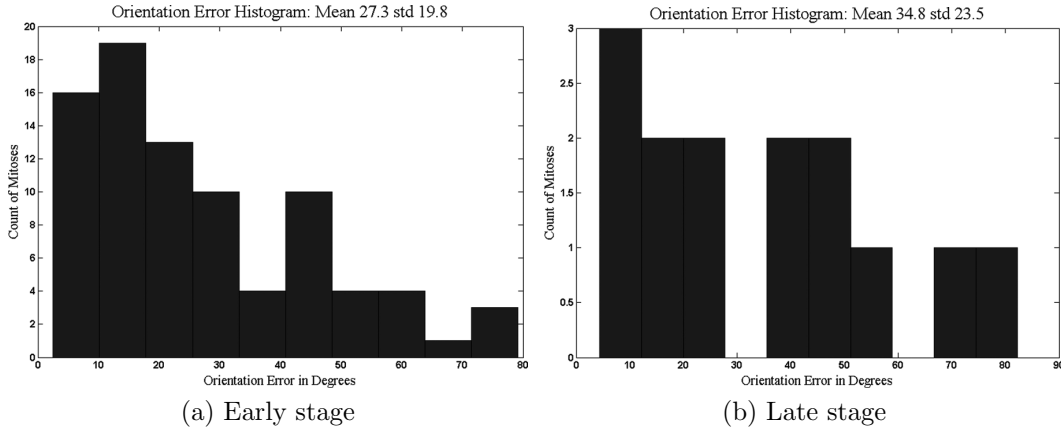


Figure 5.3: The orientation error for the mitosis detected by the motion based algorithm. The low accuracy of the orientation results are due to the sparse detection of the mitosis motion field using optical flow.

Table 5.4: Intensity Algorithm Parameters

Set	T_m	T_b	T_{SIZE}	$t_{Mitosis} - t_{NucleusDiv} + 1$	Mesh Grid Size
Early Stage	$\frac{70}{255}$	$\frac{5}{255}$	5	2	6 pixels
Late Stage	$\frac{10}{255}$	$\frac{75}{255}$	5	5	8 pixels

seen that they conform well to the *mitosis motion field prototype* Figure 5.4. Those mitoses that do not conform well to the *mitosis motion field prototype* have high orientation error Figure 5.4. The mitosis motion field that did not conform well to the *mitosis motion field prototype* is being detected as mitosis primarily by the velocity magnitude and secondly by the small contribution due to *mitosis motion field prototype* match.

5.2 Intensity Based Algorithm

For the intensity based algorithm, the parameters that must be estimated by the user are the duration of mitosis $t_{Mitosis}$, the time to the division of nucleus $t_{NucleusDiv}$ and the threshold parameters T_m , T_b , T_{SIZE} . These parameters, presented in Table 5.4, were chosen using 3 of the 94 manually detected mitoses on the early stage image set and using image sequence 2 and 3 for the late stage image set; these mitoses were not used in the testing phase. The confusion matrix for the two image sets, with the parameters presented in Table 5.4, are presented in Figure 5.5. Based on the confusion matrix results, the performance of the algorithm, using the F-Measure, on the early stage image set is 73.9% and on the late stage image set is 90.0%.

The overall performance of the algorithm can be studied from the PRC, Figure 5.6, which plots the precision and recall as a function of the different thresholds

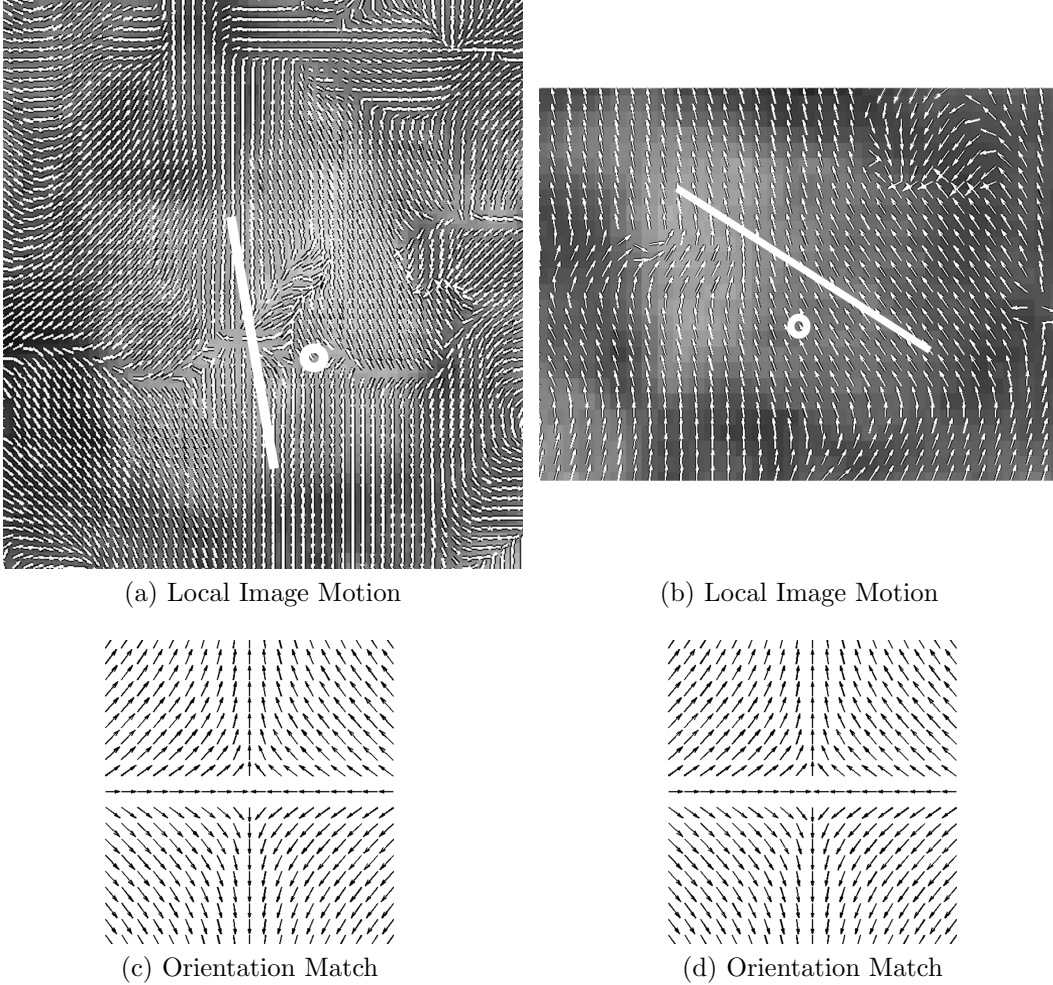


Figure 5.4: (a,b) Shows the normalized local image motion field, true orientation of mitosis (white line) and location where the orientation of the *mitosis motion field prototype* had the best match (white circle). (c,d) Illustrate the *mitosis motion field prototype* that matched with the local image motion field illustrated in (a,b). In the case of (a) the local image motion field is a good representation of the *mitosis motion field prototype*, thus the error in orientation estimate is small. In the case of (b), large scale deformation has degraded the local image motion field resulting in a large error on mitosis orientation estimate. It should be noted the match of the *mitosis motion field prototype* within (b) is less than 0.2, however since the velocity magnitude is high this location is detected as mitosis.

		Predicted				Predicted	
		Positive	Negative			Positive	Negative
Act- ual	Positive	65	26	Act- ual	Positive	18	3
	Negative	20	N/A		Negative	1	N/A

(a) Early stage

(b) Late stage

Figure 5.5: The confusion matrices for the intensity based mitosis detection algorithms on the early and late stage image sets using the optimal threshold values as determined from the data set by the author.

used in the algorithm. From the PRCs, Figure 5.6, it can be seen that the intensity algorithm performs best on the late stage image set. There are several reasons for this, but the main reason is the image quality. In the late stage image set all cells have relatively the same intensity value and the early stage image set has a wide range from very dark cells to very light cells. This causes two problems: FPs due to motion of the boundary between the dark and light cell and FNs due to difficulties in choosing the magnitude thresholds T_b and T_m .

The motion of a boundary between a dark cell and a light cell appears as a mitosis due to improper fit of the material reference frame. The material reference frame is estimated from sparse key points and thus will not deform exactly with the embryo epithelia at all locations. As illustrated in Figure 5.7, this error in the material reference frame at the boundary between light and dark cells, results in intensity changes that are detected as mitosis. The error in the material reference frame is in part due to the large deformation that occur between consecutive frames as a result of the large time span between frames and the low-magnification of the images in the early stage data set. Once again, due to the unavailability of young embryos, the algorithm could not be tested on high-magnification images of early stage embryo development.

The linear intensity drop, modeled by T_b and T_m , is insufficient to capture the intensity drop of all the different cell intensities present in the early stage image set. Some cells have a smaller intensity drop during mitosis than the value modeled by the linear intensity drop and thus were not detected as mitoses. The linear model parameters were estimated using hand marked mitosis of a very dark and two very light cells. Based on the test results, this linear model performs well when detecting mitosis of very dark and very light cells and not so well at detecting mitosis of cells with medium (gray) intensity. This suggests that perhaps a nonlinear model of intensity drops would be better than the linear model used here; the nonlinear model should have the same threshold values for dark and light cells but a lower one for the medium intensity cells.

Another reason for the poor performance of the intensity based algorithm, on the early stage image set, is the high frequency of mitoses. When the mitosis frequency is high, adjacent cells can under go mitosis at the same time. When this happens there is a tendency for the algorithm to detect multiple adjacent mitosis

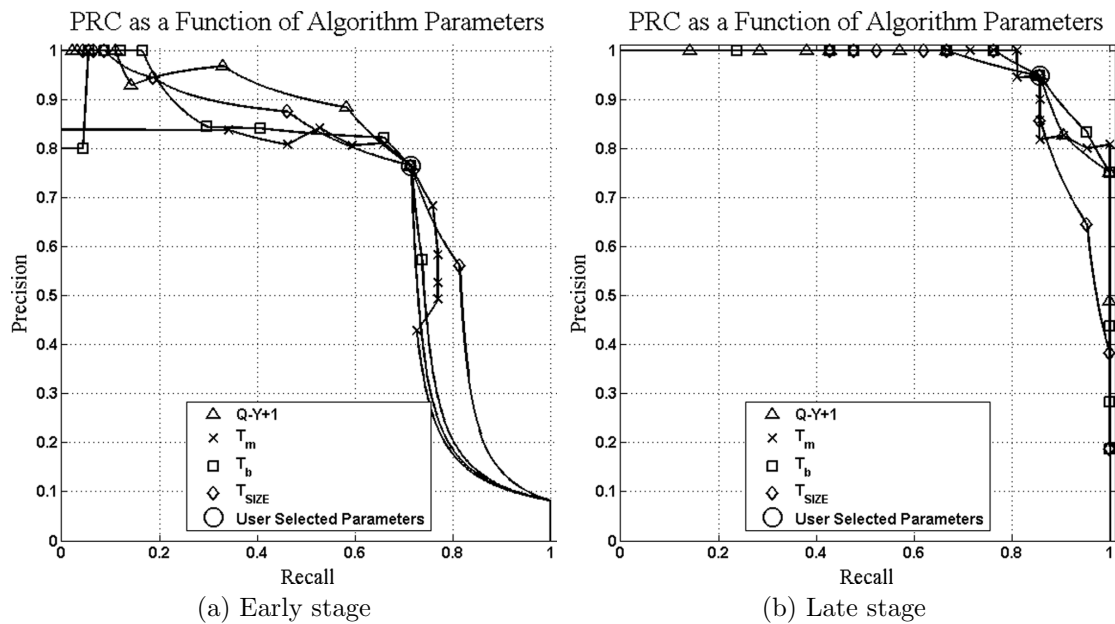


Figure 5.6: The precision-recall curves as a function of the intensity algorithm thresholds, for both the early and late stage image sets. The use of low-magnification images and the presence of high density of neighboring mitoses in the early stage image set reduces the performance of the intensity based algorithm. The intensity algorithm performs best when analyzing high-magnification images where neighboring cells are not undergoing mitosis; like those in the late stage image set.

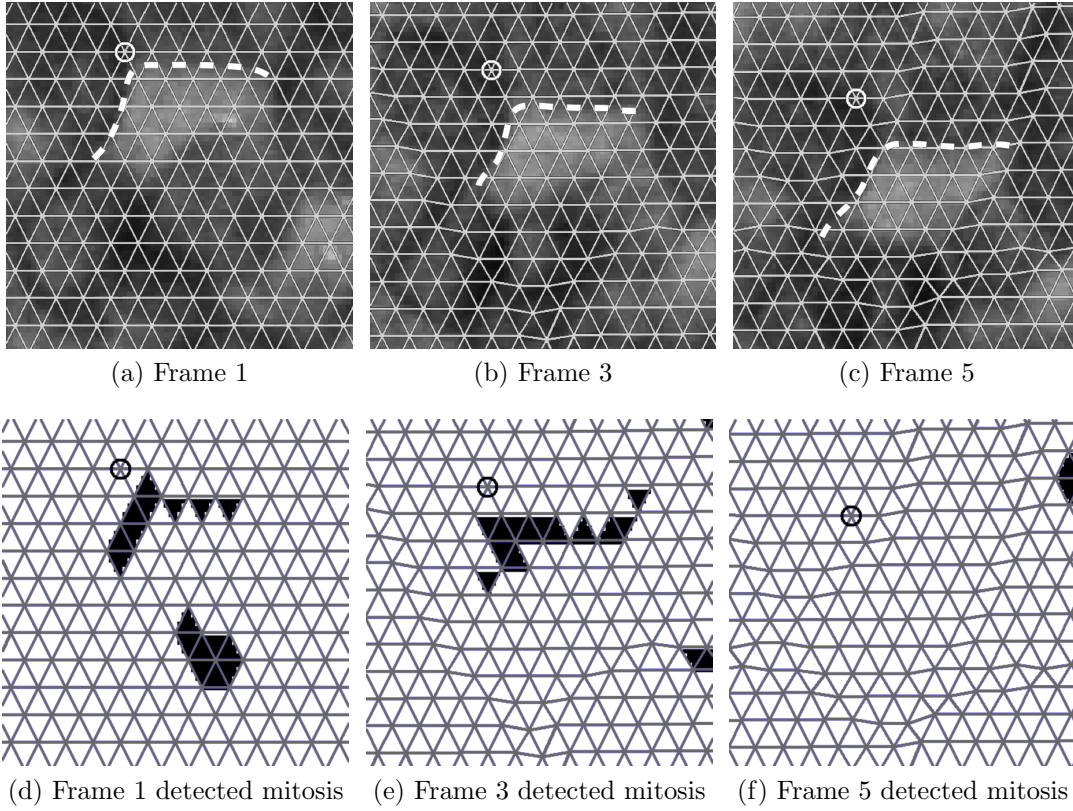


Figure 5.7: The circle is a point fixed on the material reference frame (triangular mesh). The dashed line in (a-c) is the manually marked edge boundary between a dark and light cell. From (a-c) it can be seen that the edge boundary moves relative to the material reference frame. This motion causes intensity changes on the triangular grids of the material reference frame that are still present after the applications of thresholds; as indicated by the black triangles in (d-e). The boundary motion has caused a FP because each connected black component in (d-e) are the detected mitosis. Ideally the material reference frame should deform with the epithelia and there should be no motion of the epithelia relative to the material reference frame.

as a single mitosis due to the various intensity changes occurring nearby as well as the deformation of the local area (Figure 5.8).

The histogram of the error in the orientation of the detected mitoses are presented in Figure 5.9. The early stage image set has a mean error of 39.8° with a std of 28.9° and the late stage image set has a mean error of 15.7° and a std of 18.9° . As will be seen the large error in the early image set is due to the low-magnification images used. To accurately estimate the orientation, a set of triangular grids from the material reference frame that have high intensity change must be located in a line along the diameter of the cell where the nucleus division occurs. If the number of these triangles along the cell diameter are large enough then the ellipse that is fit around these triangle will have the same orientation as the mitosis.

In the case of the early stage mitosis, due to the low-magnification images, the number of triangles that can fit within the diameter of the cell is not large enough to accurately estimate the orientation of the cell diameter as seen in Figure 5.10. The larger cells in the early stage image sets are at a large enough magnification for correct estimate of the orientation Figure 5.10. Further degradation of the orientation estimate for the early stage image set is caused by the algorithms tendency to merge neighboring mitoses.

The few large errors in the late stage image set, observed from the orientation error histogram Figure 5.9, is due to a diffused nucleus division. When the intensity drop due to nucleus division is diffused over the entire cell, as opposed to just along the cell diameter, the orientation estimation does not provide accurate information (Figure 5.11). The intensity drop is diffused over the cell as a result imaging conditions such as poor illuminations and shadows.

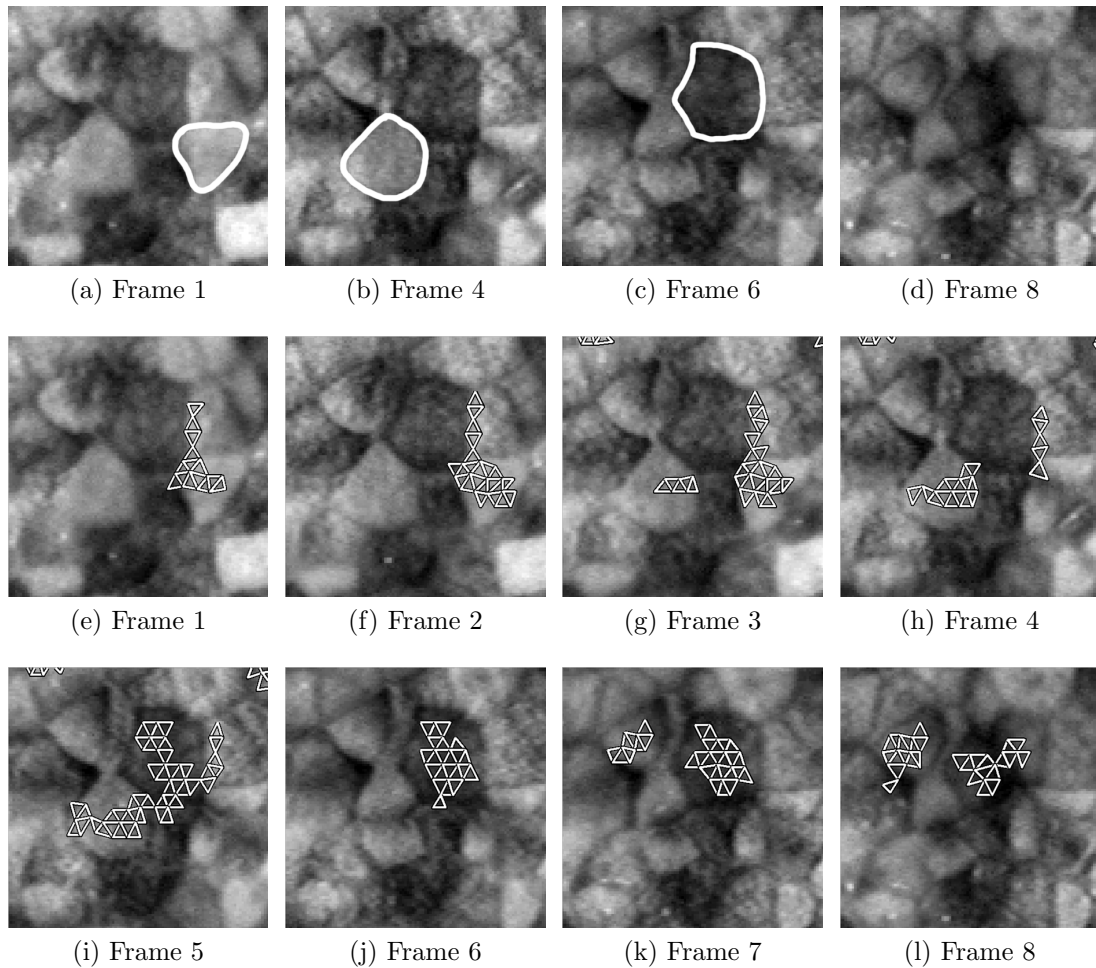


Figure 5.8: When isolating mitosis, spatially overlapping high intensity differences over multiple frames are combined as a single mitosis. This causes multiple adjacent mitoses to be detected as a single mitosis as seen in this figure. The triangle grids, of the material reference frame, that have high intensity differences are plotted on top of the epithelia images. The intensity differences of the three mitosis are joined together through the high intensity difference triangles on Frame 5 (i). The three cells that undergo mitosis, which are detected as one, are illustrated in (a-d).

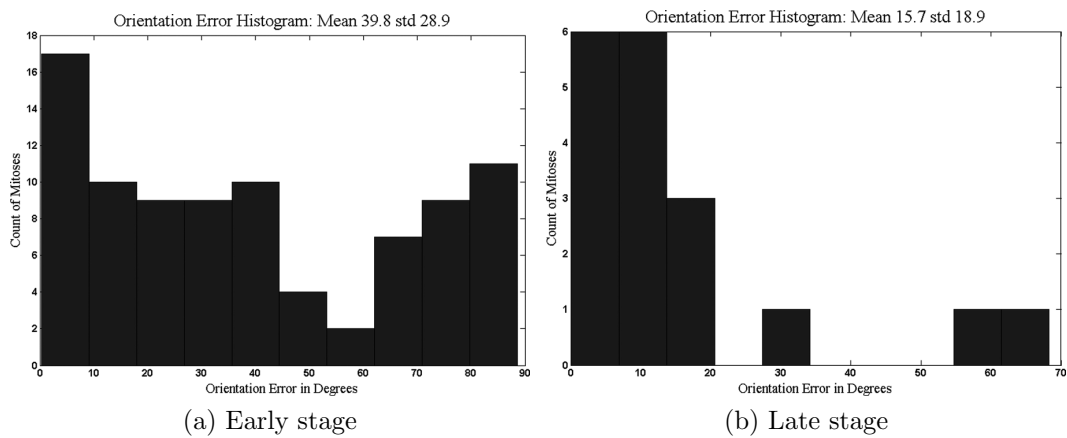


Figure 5.9: The orientation error for the mitosis detected by the intensity based algorithm. The poor performance of the early stage image set is due to the low-magnification images used. With low-magnification images a high resolution material reference frame, needed to obtain the orientation of the mitosis, can not be created.

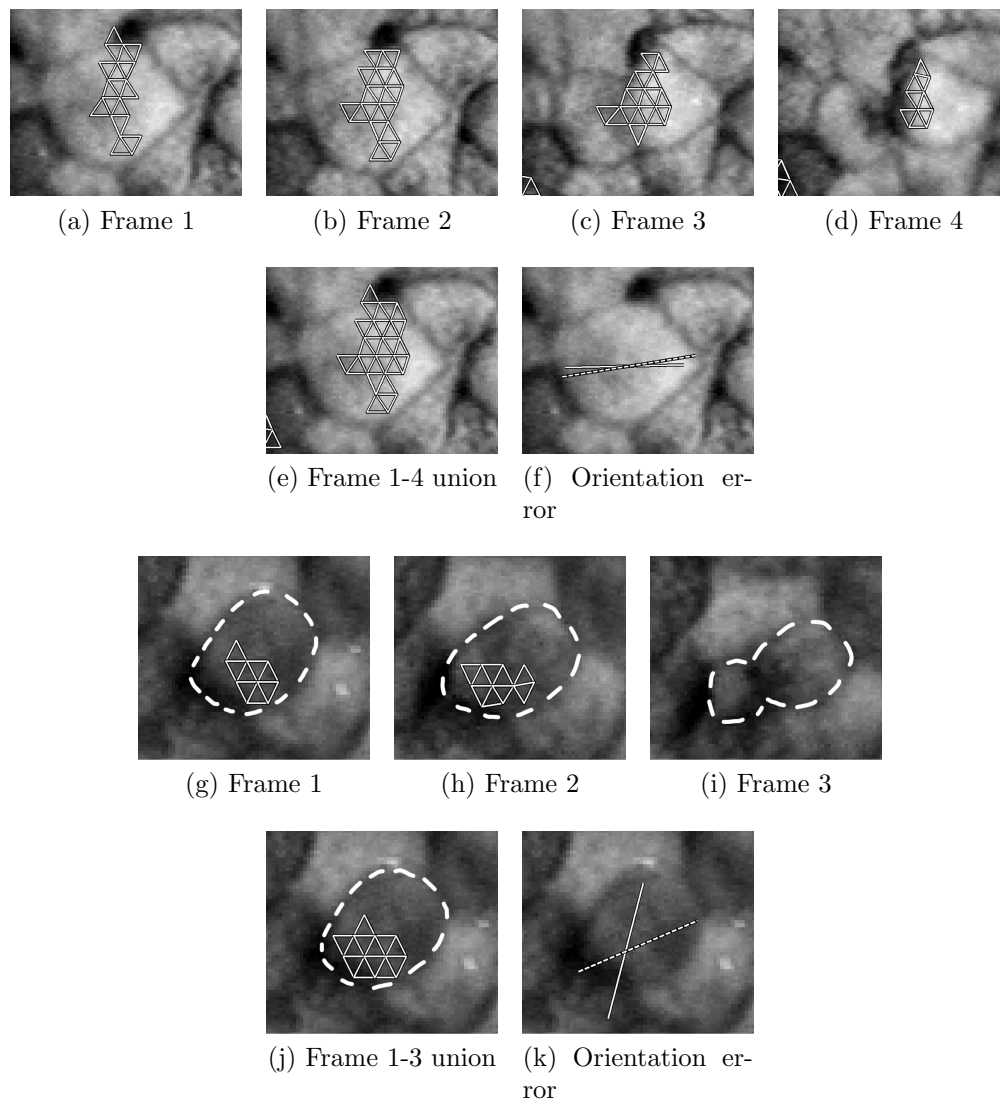


Figure 5.10: The orientation estimations for a large and small cell in the early stage image set is shown. For the large cell, the detected orientation (solid line in (f)) is close to the ground truth orientation (dashed line in (f)). For the small cell the predicted orientation is much different than the ground truth orientation (k). The reason for the high orientation error is that when the magnification is small, the number of triangles from the material reference frame that can span the diameter of the cell is too few.

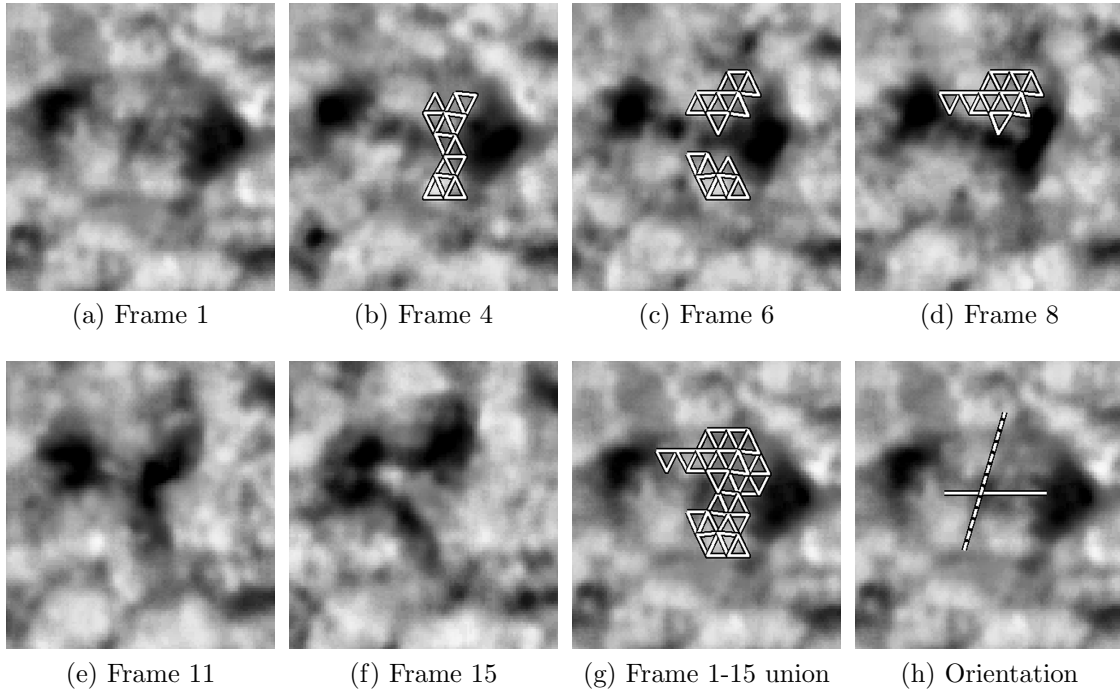


Figure 5.11: During nucleus division, the intensity drop will normally occur linearly along the cell diameter. Sometimes, like in the case illustrated here, the intensity drop will be partially or totally diffused and will no longer appear linear. In the case illustrated here, a larger area on the right side of the cell drops in intensity than on the left side of the cell. As a result of this, the triangular grids with high intensity drops are localized on the right side of the cell as seen on (g). This will give a very large error in the estimate of the mitosis orientation as seen on (h); solid line represent the detected orientation, dashed line represent the ground truth orientation.

Chapter 6

Conclusions and Future Work

Embryogenesis consists of three types of processes: mitosis, cell differentiation and morphogenetic movements. It has been shown that the frequency and orientation of mitosis can affect morphogenetic movements. To study the effect of mitosis on morphogenetic movements, an automatic algorithm for counting mitoses on time lapse images of embryo epithelia is needed. This thesis presented two algorithms for counting mitosis in time-lapse images of embryo epithelia; a motion based and an intensity based algorithm. A comparison of these two methods to existing algorithms is not possible as, to the best of the author's knowledge, no automatic algorithms for detecting mitosis on live tissue exists in the literature.

Low-magnification, early stage embryo development image set and high-magnification, late stage embryo development image set were used to test these algorithms. Unfortunately, due to lack of young embryos, high-magnification early stage embryo development image sets could not be obtained at this time. The mitosis location and orientation in these two image sets were manually determined for testing.

The motion based algorithm had performance rates of 68.2% on early stage image set and 66.7% on late stage image set, where as the intensity based algorithm had a performance rates of 73.9% on early stage image set and 90.0% on late stage image set. The mitosis orientation errors for the motion based algorithm were 27.3° average error with a standard deviation of 19.8° for early stage set and 34.8° average with a standard deviation of 23.5° for the late stage set. For the intensity based algorithm the orientation errors were 39.8° average with standard deviation of 28.9° for the early stage image set and 15.7° average with standard deviation of 18.9° for the late stage image set.

Under low magnification the motion based algorithm performs poorly due to the presence of large scale epithelia reshaping. The intensity based algorithm is also affected by the presence of large scale reshaping, but not as significantly as the motion based algorithm. Using high-magnification images the motion due to large scale reshaping is minimized but noise levels and illumination defects are increased. As a result the motion based algorithm still has low performance, whereas the

intensity based algorithm is robust to the noise and illumination changes that occur at the high-magnification images.

Based on these results, the performance of the intensity based algorithm is much better than the motion based algorithm. The intensity based algorithm will work best when high-magnification images, where all the cells have approximately the same average intensity, are used. The algorithm will work best for late stage embryo development images where it is less likely to have neighboring cells undergo mitosis at the same time because the algorithm will detect neighboring mitosis as a single mitosis. To fully understand the performance of the intensity based algorithm it is desirable to study its performance on high-magnification images of early stage embryo development.

There are still several areas left to be explored to improve the intensity based algorithm. First and foremost, the detection of adjacent mitosis must be explored. One method of separating several mitosis detected as a single mitosis is to use average cell size with cell boundary information. That is, if the detected mitosis occupies an area much larger than the average cell size then local edge information can be used to split the detected mitosis area into several mitosis areas.

A second area for improvement is the definition of the magnitude of the intensity drop during mitosis as a function of cell average intensity. The currently used linear model of intensity drop has shown to be inaccurate at estimating the intensity drop of all cells. A study using images of multiple embryos (pigmentation varies between embryos) is needed to determine the best model for this function.

A third area for improvement is the estimation of the mitosis orientation. While the method presented here has performed well for high-magnification images the performance can still be improved. Other means of detecting orientation, not explored in this thesis, must be studied to determine the best means of estimating mitosis orientation. One potential method is to determine the newly formed cell boundary between the two daughter cells.

Finally, while the presented algorithm is the only automated algorithm currently available for detecting mitosis on live tissue, it still requires a certain amount of manual intervention. The presented algorithm needs a few manually detected mitoses to determine threshold parameters. It is desirable to determine an automated means of selecting these thresholds. Unfortunately, since the pigmentation varies between embryos it is not known whether an automated means of selecting thresholds is possible.

Appendix A

Optical Flow Algorithm

Singh's optical flow method [44] first estimates a coarse velocity vector at each pixel by taking a region of interest (ROI) in frame t and matching it to the next frame by minimizing the sum of squared difference (SSD) within a search window. In this thesis, minimizing the SSD method for local region matching was replaced by maximizing the normalized cross-correlation, since normalized cross-correlation was already implemented for determining global translations (Section 3.2). Using the normalized cross-correlation, an n by n ROI around each image pixel was matched to the next frame using a search window of size N by N pixels. The resulting N by N normalized cross-correlation at image pixel (x, y) is obtained as

$$\mathbf{N}_{cc}(u, v) = \frac{\sum_{i,j=-\frac{n-1}{2}}^{\frac{n-1}{2}} [I_2(x-u-i, y-v-i) - \overline{I_2(x-u, y-v)}][I_1(x-i, y-j) - \overline{I_1(x, y)}]}{\sqrt{\sum_{i,j=-\frac{n-1}{2}}^{\frac{n-1}{2}} [I_2(x-u-i, y-v-i) - \overline{I_2(x-u, y-v)}]^2 \sum_{i,j=-\frac{n-1}{2}}^{\frac{n-1}{2}} [I_1(x-i, y-j) - \overline{I_1(x, y)}]^2}} \quad (\text{A.1})$$

$$u, v = -\frac{N-1}{2} \dots \frac{N-1}{2}$$

Where $\overline{I_1(x, y)}$ and $\overline{I_2(x-u, y-v)}$ are the average intensity in the n by n ROI around image coordinate (x, y) in frame one and $(x-u, y-v)$ in frame two.

Typically the minimum location of SSD is obtained as the new location of the tracked pixel, however, Singh uses a weighted average. Following this methodology, in this study, \mathbf{N}_{cc} is weighted as

$$\mathfrak{R}_c(u, v) = e^{-k\mathbf{N}_{cc}(u, v)} \quad (\text{A.2})$$

where $k = 7$ was obtained experimentally to produce the best results. The velocity of the tracked pixel is then obtained as the average of the weighted \mathbf{N}_{cc} ,

$$\vec{v}_{cc} = (u_{cc}, v_{cc}) = \frac{1}{\sum_{i,j=-\frac{N-1}{2}}^{\frac{N-1}{2}} \mathfrak{R}_c(i,j)} \left(\sum_{i,j=-\frac{N-1}{2}}^{\frac{N-1}{2}} \mathfrak{R}_c(i,j)i, \sum_{i,j=-\frac{N-1}{2}}^{\frac{N-1}{2}} \mathfrak{R}_c(i,j)j \right) \quad (\text{A.3})$$

The displacement vectors obtained from Eq. A.3 is used as the coarse estimate of the optical flow field \mathcal{U}_{cc} . The covariance of the matched result is obtained as

$$\mathbf{S}_{cc} = \frac{1}{\sum_{i,j=-\frac{N-1}{2}}^{\frac{N-1}{2}} \mathfrak{R}_c(i,j)} \begin{bmatrix} \sum_{i,j=-\frac{N-1}{2}}^{\frac{N-1}{2}} \mathfrak{R}_c(i,j)(i-u_{cc})^2 & \sum_{i,j=-\frac{N-1}{2}}^{\frac{N-1}{2}} \mathfrak{R}_c(i,j)(i-u_{cc})(j-v_{cc}) \\ \sum_{i,j=-\frac{N-1}{2}}^{\frac{N-1}{2}} \mathfrak{R}_c(i,j)(i-u_{cc})(j-v_{cc}) & \sum_{i,j=-\frac{N-1}{2}}^{\frac{N-1}{2}} \mathfrak{R}_c(i,j)(j-v_{cc})^2 \end{bmatrix} \quad (\text{A.4})$$

The coarse estimate of the velocity field obtained using Eq. A.3, \mathcal{U}_{cc} , estimates the velocity of each pixel independent from its neighboring pixels. Singh argues that, for cases where the pixel of interest is not on a motion boundary, the velocity of a pixel will be similar to that of its neighbors. Based on this Singh concludes that a Gaussian weighted average velocity of a local neighborhood around a pixel will be similar to the actual velocity of the pixel. That is, given the true image velocity field $\mathcal{U} = (\mathbf{u}_t, \mathbf{v}_t)$, the average velocity field $\bar{\mathcal{U}}$ and its corresponding covariance matrix are obtained by Eqs. A.5 and A.6 using \mathfrak{R}_n . \mathfrak{R}_n is a W by W Gaussian weighting window.

$$\begin{aligned} \vec{v}_{avg}(x,y) &= (\mathbf{u}_{avg}(x,y), \mathbf{v}_{avg}(x,y)) \\ &= \frac{1}{\sum_{i,j=-\frac{W-1}{2}}^{\frac{W-1}{2}} \mathfrak{R}_n(i,j)} \left(\sum_{i,j=-\frac{W-1}{2}}^{\frac{W-1}{2}} \mathfrak{R}_n(i,j)\mathbf{u}_t(x-i,y-j), \sum_{i,j=-\frac{W-1}{2}}^{\frac{W-1}{2}} \mathfrak{R}_n(i,j)\mathbf{v}_t(x-i,y-j) \right) \end{aligned} \quad (\text{A.5})$$

$$\mathbf{S}_n(x,y) = \frac{1}{\sum_{i,j=-\frac{W-1}{2}}^{\frac{W-1}{2}} \mathfrak{R}_n(i,j)} \begin{bmatrix} \sum_{i,j=-\frac{W-1}{2}}^{\frac{W-1}{2}} \mathfrak{R}_n(i,j)a & \sum_{i,j=-\frac{W-1}{2}}^{\frac{W-1}{2}} \mathfrak{R}_n(i,j)b \\ \sum_{i,j=-\frac{W-1}{2}}^{\frac{W-1}{2}} \mathfrak{R}_n(i,j)b & \sum_{i,j=-\frac{W-1}{2}}^{\frac{W-1}{2}} \mathfrak{R}_n(i,j)c \end{bmatrix} \quad (\text{A.6})$$

$$\begin{aligned} a &= (\mathbf{u}_t(x-i,y-j) - \mathbf{u}_{avg}(x,y))^2 \\ b &= (\mathbf{u}_t(x-i,y-j) - \mathbf{u}_{avg}(x,y))(\mathbf{v}_t(x-i,y-j) - \mathbf{v}_{avg}(x,y)) \\ c &= (\mathbf{v}_t(x-i,y-j) - \mathbf{v}_{avg}(x,y))^2 \end{aligned}$$

Based on the two estimates of the velocity fields, \mathcal{U}_{cc} and $\bar{\mathcal{U}}$, Singh obtains the true velocity field, \mathcal{U} , as the one that minimizes the following error norms.

$$\begin{aligned}
E = \int \int & [(\mathcal{U}(x, y) - \bar{\mathcal{U}}(x, y))^T \mathbf{S}_n^{-1}(x, y)(\mathcal{U}(x, y) - \bar{\mathcal{U}}(x, y)) \\
& + (\mathcal{U}(x, y) - \mathcal{U}_{cc}(x, y))^T \mathbf{S}_{cc}^{-1}(x, y)(\mathcal{U}(x, y) - \mathcal{U}_{cc}(x, y))] dx dy
\end{aligned} \tag{A.7}$$

This leads to the following condition for the optimal solution

$$\mathbf{S}_{cc}^{-1}(x, y)[\mathcal{U}(x, y) - \mathcal{U}_{cc}(x, y)] + \mathbf{S}_n^{-1}(x, y)[\mathcal{U}(x, y) - \bar{\mathcal{U}}(x, y)] = 0 \tag{A.8}$$

Since \mathcal{U} , $\bar{\mathcal{U}}$ and \mathbf{S}_n are unknown, Eq. A.8 can not be solved directly. However, Singh provides us with an iterative solution to Eq. A.8 as

$$\begin{aligned}
\mathcal{U}^{k+1}(x, y) &= [\mathbf{S}_{cc}^{-1}(x, y) + \mathbf{S}_n^{-1}(x, y)]^{-1} [\mathbf{S}_{cc}^{-1}(x, y)\mathcal{U}_{cc}(x, y) + \mathbf{S}_n^{-1}(x, y)\bar{\mathcal{U}}^k] \\
\mathcal{U}^0 &= \mathcal{U}_{cc}
\end{aligned} \tag{A.9}$$

Appendix B

Triangular Mesh

A triangular mesh, as illustrated in Figure B.1, can be thought of as an alternative to the rectangular meshes that are typically used to represent images. While this coordinate system is beneficial in tracking deformable objects [34, 35, 38, 39, 47], mathematical formulations are needed for converting between the triangular mesh and the rectangular mesh images.

The triangular mesh is represented by a set of vertices, $\mathbf{S} = \{\underline{v}_1, \dots, \underline{v}_L\}$, in the image coordinate frame as illustrated in Figure B.1. The triangles in the mesh are indexed in a row major fashion from the top left. The intensity value of a triangle is defined as the average intensity of the image pixel centers that are located in the triangle. For example the shaded image pixels in Figure B.1 represents the intensity of triangle 2 ($G(2)$).

Another term to be defined on a triangular mesh is pixel connectivity. In a square grid, pixel connectivity is defined as either 4-connected or 8-connected as illustrated in Figure B.2a. This is useful when classifying a single object in a binary image as either 8- or 4-connected object. In a similar manner, in the triangular mesh connectivity can be defined as 3-connected or 12-connected as illustrated in Figure B.2b. In this thesis all connected objects on triangular mesh are composed of 12-connected triangles.

B.1 Derivative Constraint on Mesh Vertices

In tracking triangular meshes, the regular triangular mesh shown in Figure B.3a is allowed to deform between frames; the result is a non-regular triangular mesh. To limit the amount of deformation between frames a smoothness constraint is introduced on the meshes vertices. The smoothness constraint is a the second derivative constraint on all adjacent vertex triplets laying along the mesh line (Figure B.3b). By minimizing the square of the second derivative between all vertex triplets, it can be ensured that the deformation is limited between frames.

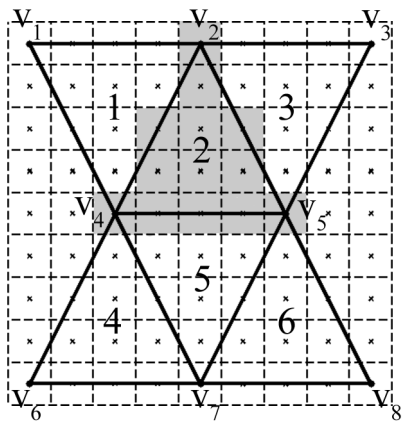


Figure B.1: A triangular mesh on an image is represented by its vertices v_1, \dots, v_8 . The triangles are indexed from left to right. The intensity of a triangle is the average intensity of all pixels within the triangle as illustrated by the shaded area for triangle 2.

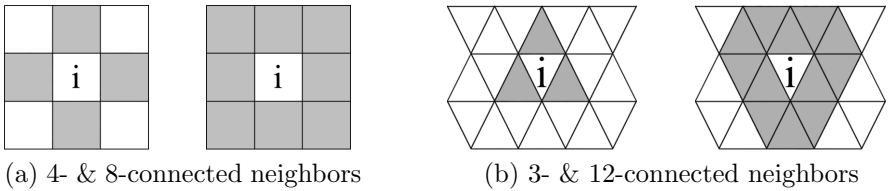


Figure B.2: (a) The two type of grid connectivity on a square grid. (b) The two type of grid connectivity on a triangular grid.

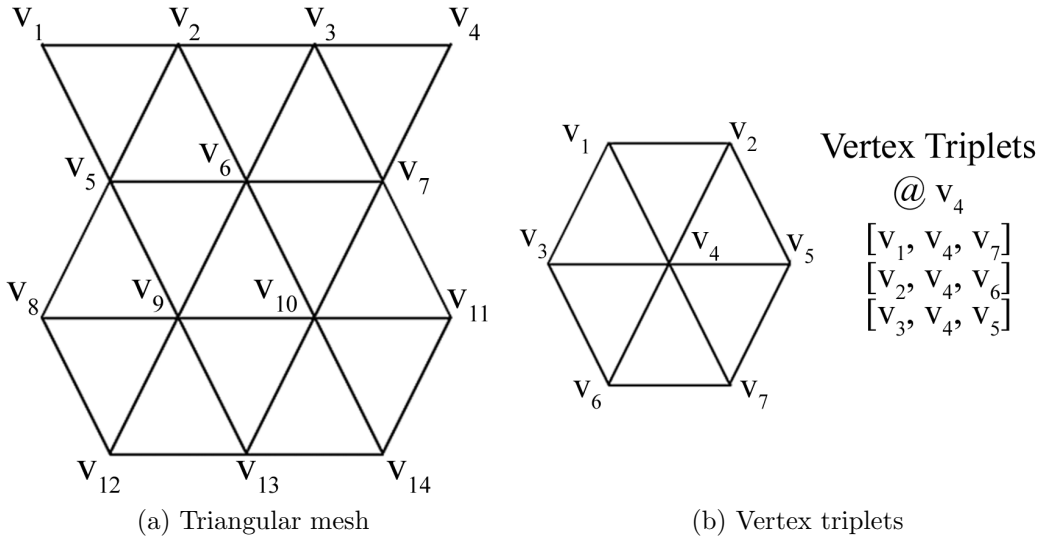


Figure B.3: (a) A triangular mesh with vertices labeled. (b) All vertex triplets at a given vertex (v_4).

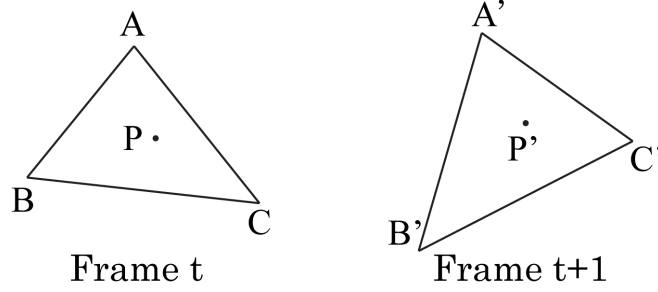


Figure B.4: A triangle in the mesh at Frame t is deformed to Frame $t + 1$. Given the location of the vertices (A, B, C) and (A', B', C') in frame t and $t + 1$, the point P from frame t needs to be mapped to frame $t + 1$ relative to the triangle vertices.

The second derivative constraint is represented by a banded matrix \mathbf{K}' , where each row represents one vertex triplet and each column represents a vertex on the mesh. Each row will approximate the second derivative using the filter $[-1 \ 2 \ -1]$. The second derivative constraint matrix \mathbf{K}' for the mesh in Figure B.3a is

$$\mathbf{K}' = \begin{pmatrix} -1 & 2 & -1 & 0 & 0 & 0 & 0 & 0 & 0 & 0 & 0 & 0 & 0 & 0 \\ 0 & -1 & 2 & -1 & 0 & 0 & 0 & 0 & 0 & 0 & 0 & 0 & 0 & 0 \\ -1 & 0 & 0 & 0 & 2 & 0 & 0 & 0 & -1 & 0 & 0 & 0 & 0 & 0 \\ 0 & -1 & 0 & 0 & 2 & 0 & 0 & -1 & 0 & 0 & 0 & 0 & 0 & 0 \\ 0 & 0 & -1 & 0 & 0 & 2 & 0 & 0 & -1 & 0 & 0 & 0 & 0 & 0 \\ 0 & 0 & 0 & 0 & -1 & 2 & -1 & 0 & 0 & 0 & 0 & 0 & 0 & 0 \\ 0 & 0 & -1 & 0 & 0 & 0 & 2 & 0 & 0 & 0 & -1 & 0 & 0 & 0 \\ 0 & 0 & 0 & -1 & 0 & 0 & 2 & 0 & 0 & -1 & 0 & 0 & 0 & 0 \\ 0 & 0 & 0 & 0 & -1 & 0 & 0 & 2 & 0 & 0 & 0 & 0 & -1 & 0 \\ 0 & 0 & 0 & 0 & 0 & -1 & 0 & 0 & 2 & 0 & 0 & -1 & 0 & 0 \\ 0 & 0 & 0 & 0 & 0 & 0 & -1 & 2 & -1 & 0 & 0 & 0 & 0 & 0 \\ 0 & 0 & 0 & 0 & 0 & 0 & -1 & 0 & 0 & 2 & 0 & 0 & 0 & -1 \\ 0 & 0 & 0 & 0 & 0 & 0 & 0 & -1 & 0 & 0 & 2 & 0 & 0 & -1 \\ 0 & 0 & 0 & 0 & 0 & 0 & 0 & 0 & -1 & 2 & -1 & 0 & 0 & 0 \\ 0 & 0 & 0 & 0 & 0 & 0 & 0 & 0 & 0 & 0 & 0 & -1 & 2 & -1 \end{pmatrix} \quad (\text{B.1})$$

The square of the second derivative is obtained as $\mathbf{K} = \mathbf{K}'^T \mathbf{K}'$.

B.2 Barycentric Coordinates

A triangle, on the triangular mesh, will deform between two frames as illustrated in Figure B.4. Any point, \underline{P} , inside this triangle can be transformed from the one frame to the next relative to the triangle vertices using barycentric coordinates. Barycentric coordinates were introduced by August Ferdinand Möbius in 1827 [16].

In barycentric coordinates a point \underline{P} is represented by the barycentric triplet $(\lambda_1, \lambda_2, \lambda_3)$, which are weights needed on the triangle vertices $(\underline{A}, \underline{B}, \underline{C})$ to make point \underline{P} the center of mass of the triangle. Only the ratio between the weights are important in representing the point \underline{P} , as a result the constraint $\lambda_1 + \lambda_2 + \lambda_3 = 1$ is enforced. The cartesian coordinate of \underline{P} is then represented using the coordinates of the triangle vertices as

$$\underline{P} = \lambda_1 \underline{A} + \lambda_2 \underline{B} + \lambda_3 \underline{C} \quad (\text{B.2})$$

Solving for the triplet $(\lambda_1, \lambda_2, \lambda_3)$, yields

$$\lambda_1 = \frac{(B_x - C_x)(C_y - P_y) - (C_x - P_x)(B_y - C_y)}{(A_x - C_x)(B_y - C_y) - (B_x - C_x)(A_y - C_y)} \quad (\text{B.3})$$

$$\lambda_2 = \frac{(A_x - C_x)(C_y - P_y) - (C_x - P_x)(A_y - C_y)}{(B_x - C_x)(A_y - C_y) - (A_x - C_x)(B_y - C_y)} \quad (\text{B.4})$$

$$\lambda_3 = 1 - \lambda_1 - \lambda_2 \quad (\text{B.5})$$

Given the barycentric triplets from the first frame $(\lambda_1, \lambda_2, \lambda_3)$ and the location of the triangle vertices in the second frame $(\underline{A}', \underline{B}', \underline{C}')$ the location of point \underline{P} in the second frame can be obtained using Eq. B.2.

List of References

- [1] J. B. Armstrong and G. M. Malacinski. *Developmental Biology of the Axolotl*. Oxford University Press, 1989. 2, 41
- [2] J. L. Barron, D. J. Fleet, and S. S. Beauchemin. Performance of optical flow techniques. *International Journal of Computer Vision*, 12(1):43–77, February 1994. 19
- [3] R. Benko and G. W. Brodland. Measurement of in vivo stress resultants in neurulation-stage amphibian embryos. *Annals of Biomedical Engineering*, 35(4):672–681, 2007. 2
- [4] L. Bertucco, G. Nunnari, C. Randieri, V. Rizza, and A. Sacco. A cellular neural network based system for cell counting in culture of biological cells. In *Proceedings of the IEEE International Conference on Control Applications*, volume 1, pages 341–345, Trieste, Italy, September 1998. 5
- [5] L. D. Botto, C. A. Moore, M. J. Khoury, and J. D. Erickson. Neural-tube defects. *The New England Journal of Medicine*, 341:1509–1519, 1999. 1, 2
- [6] G. W. Brodland, D. I. L. Chen, and J. H. Veldhuis. A cell-based constitutive model for embryonic epithelia and other planar aggregates of biological cells. *International Journal of Plasticity*, 22:965–995, 2006. 2
- [7] G. W. Brodland and J. H. Veldhuis. Computer simulations of mitosis and interdependencies between mitosis, cell shape and epithelium reshaping. *Journal of Biomechanics*, 35:673–681, 2002. 2, 3, 16
- [8] M. R. Brouns and H. W. M. van Straaten. Models of neural tube defects. *Drug Discovery Today: Disease Models*, 2(4):285–290, 2005. 1, 2
- [9] Y. M. Chen, K. Biddell, A. Y. Sun, P. A. Relue, and J. D. Johnson. An automatic cell counting method for optical images. In *Proceedings of The First Joint BMES/EMBS Conference*, volume 2, page 819, Atlanta, GA, USA, October 1999. 5
- [10] D. A. Clausi and G. W. Brodland. Mechanical evaluation of theories of neurulation using computer simulation. *Development*, 118:1013–1023, 1993. 2

- [11] A. J. Copp, F. A. Brook, J. P. Estibeiro, A. S. W. Shum, and D. L. Cockroft. The embryonic development of mammalian neural tube defects. *Progress in Neurobiology*, 35:363–403, 1990. 1, 2
- [12] S. S. Cross and R. D. Start. Estimating mitotic activity in tumors. *Histopathology*, 29:485–488, 1996. 7, 8
- [13] J. Davis and M. Goadrih. The relationship between precision-recall and roc curves. In *23rd International Conference on Machine Learning*, volume 148, pages 233–240, 2006. 42
- [14] E. R. Dougherty and R. A. Lotufo. *Hands-on morphological image processing*. SPIE Press, 2003. 22, 32
- [15] J. Ebling and G. Scheuermann. Clifford convolution and pattern matching on vector fields. In *Proceedings of IEEE Visualization*, pages 193–200, Los Alamitos, CA, USA, 2003. 20
- [16] J. Fauvel, R. Flood, and R. Wilson. *Mobius and his band: Mathematics and Astronomy in Nineteenth-century German*. Oxford University Press, 1993. 63
- [17] A. Fedorov, N. Chrisochoides, R. Kikinis, and K. Warfield. An evaluation of three approaches to tetrahedral mesh generation for deformable registration of brain mr images. In *Proceedings of the 3rd IEEE International Symposium on Biomedical Imaging*, pages 658–661, 2006. 26
- [18] D. J. Fleet, A. D. Jepson, and M. R. M. Jenkin. Phase-based disparity measurement. *Computer Vision, Graphics, and Image Processing. Image Understanding*, 53(2):198–210, 1991. 11
- [19] P. Fua and Y. G. Leclerc. Object-centered surface reconstruction: Combining multi-image stereo and shading. *International Journal of Computer Vision*, 16:35–56, 1995. 26
- [20] R. Gal, L. Rath-Wolfson, Y. Rosenblatt, M. Halpern, A. Schwartz, and R. Koren. An improved technique for mitosis counting. *International Journal of Surgical Pathology*, 13(2):161–165, 2005. 8
- [21] R. C. Gonzalez, R. E. Woods, and S. L. Eddins. *Digital Image Processing Using MATLAB*. Prentice Hall, 2004. 22
- [22] E. B. Heiberg. *Automated feature detection in multidimensional images*. PhD thesis, Linkpings Universitet, 2004. 20
- [23] B. K. P. Horn and B. G. Schunck. Determining optical flow. *Artificial Intelligence*, 17(1-3):185–203, August 1981. 19
- [24] W. Hu, T. Tan, L. Want, and S. Maybank. A survey on visual surveillance of object motion and behaviours. *IEEE Transactions on Systems, Man, and Cybernetics*, 34(3):334–352, 2004. 9

- [25] P. Iles. Average cell orientation, eccentricity and size from tissue images. Master's thesis, University of Waterloo, Waterloo, Ontario, Canada. 6, 7, 8, 20, 38, 41
- [26] E. J. Kaman, A. W. M Smeulders, P. W. Verbeek, I. T. Young, and J. P. A. Baak. Image processing for mitoses in sections of breast cancer: A feasibility study. *Cytometry*, 5(3):244–249, 1984. 8
- [27] T. K. ten Kate, J. A. M. Belien, A. W. M. Smeulders, and J. P. A. Baak. Method for counting mitoses by image processing in feulgen stained breast cancer sections. *Cytometry*, 14(3):241–250, 1993. 8, 9, 24
- [28] S. Mahadevan and D. P. Casasent. Detection of triple junction parameters in microscope images. *SPIE*, 4387:204–214, 2001. 32
- [29] J. B. A. Maintz and M. A. Viergever. A survey of medical image registration. *Medical Image Analysis*, 2(1):1–36, 1998. 19
- [30] C. D. Manning, P. Raghavan, and H. Schtze. *Introduction to Information Retrieval*. Cambridge University Press, 2008. www-csli.stanford.edu/~schuetze/information-retrieval-book.html Accessed Sept. 2007 (In Press). 41, 42
- [31] P. Oakeshott and G. M. Hunt. Long-term outcome in open spina bifida. *The British Journal of General Practice*, 53(493):632–636, 2003. 1
- [32] L. Parida, D. Geiger, and R. Hummel. Junctions: Detection, classification, and reconstruction. *IEEE Transactions on Pattern Analysis and Machine Intelligence*, 20(7):687–698, 1998. 32
- [33] P. Phukpattaranont and P. Boonyaphiphat. An automatic cell counting method for a microscopic tissue image from breast cancer. In *IFMBE Proceedings of the 3rd Kuala Lumpur International Conference on Biomedical Engineering*, volume 15, pages 241–244, Kuala Lumpur, Malaysia, December 2006. 5, 7
- [34] J. Pilet, V. Lepetit, and P. Fua. Real-time non-rigid surface detection. In *IEEE Computer Society Conference on Computer Vision and Pattern Recognition (CVPR)*, volume 1, pages 822–828, 2005. 26, 61
- [35] J. Pilet, V. Lepetit, and P. Fua. Fast non-rigid surface detection, registration and realistic augmentation. *International Journal of Computer Vision*, January 2007. (Accepted). 26, 27, 61
- [36] A. R. Rao and R. C. Jain. Computerized flow field analysis: oriented texture fields. *IEEE Transactions on Pattern Analysis and Machine Intelligence*, 14(7):693–709, 1992. 20

- [37] H. H. Refai, L. Li, T. K. Teague, and R. Naukam. Automatic count of hepatocytes in microscopic images. In *International Conference on Image Processing*, volume 2, pages 1101–1104, Barcelona, Spain, 2003. 5
- [38] S. Sclaroff and J. Isidoro. Active blobs. In *Sixth International Conference on Computer Vision*, pages 1146–1153, 1998. 26, 61
- [39] S. Sclaroff and J. Isidoro. Active blobs: region-based deformable appearance models. *Computer Vision and Image Understanding*, 89:197–225, 2003. 26, 61
- [40] P. Shannon. Estimating bulk geometrical properties of cellular structures. Master’s thesis, University of Waterloo, Waterloo, Ontario, Canada. 6
- [41] T. Shimada, K. Kato, T. Kamikouchi, and K. Ito. Analysis of the distribution of the brain cells on the fruit fly by an automatic cell counting algorithm. *Physica A*, 350:144–149, 2005. 5
- [42] C. F. Shu and R. C. Jain. Vector field analysis for oriented patterns. *IEEE Transactions on Pattern Analysis and Machine Intelligence*, 16(9):946–950, 1994. 18, 20
- [43] J. F. Simpson, P. L. Dutt, and D. L. Page. Expression of mitoses per thousand cells and cell density in breast carcinomas: a proposal. *Human Pathology*, 23:608–611, 1992. 8
- [44] A. Singh. *Optic Flow Computation: A Unified Perspective*. IEEE Press, 1990. 19, 30, 58
- [45] A. Sluzek. A local algorithm for real-time junction detection in contour images. In *9th International Conference on Computer Analysis of Image and Patterns*, pages 465–472, 2001. 32
- [46] A. Talukder and D. P. Casasent. Multiscale gabor wavelet fusion for edge detection in microscopy images. *SPIE*, 3391(1):336–347, 1998. 6, 7, 29, 30
- [47] H. Tao and T. S. Huang. Connected vibrations: A modal analysis approach for non-rigid motion tracking. In *IEEE Computer Society Conference on Computer Vision and Pattern Recognition (CVPR)*, pages 735–740, 1998. 26, 61
- [48] H. J. ten Donkelaar, M. Lammens, and A. Hori. *Clinical Neuroembryology: Development and Developmental Disorders of the Human Central Nervous System*. Springer Berlin Heidelberg, 2006. 1, 2
- [49] S. Thrun, W. Burgard, and D. Fox. *Probabilistic Robotics*. The MIT Press, 2005. 9, 12, 13
- [50] P. J. van Diest and et al. Reproducibility of mitosis counting in 2,469 breast cancer specimens: Results from multicenter morphometric mammary carcinoma project. *Human Pathology*, 23:603–607, 1992. 8

- [51] J. H. Veldhuis and G. W. Brodland. A deformable block-matching algorithm for tracking epithelial cells. *Image and Vision Computing*, 17:905–911, 1999. 11, 26
- [52] J. H. Veldhuis, G. W. Brodland, C. J. Wiebe, and G. J. Bootsma. Multiview robotic microscope reveals the in-plane kinematics of amphibian neurulation. *Annals of Biomedical Engineering*, 33(6):821–828, 2005. 2
- [53] L. M. Vincent and B. R. Masters. Morphological image processing and network analysis of cornea endothelial cell images. *SPIE*, 1769:212–226, 1992. 6, 7
- [54] C. J. Wiebe and G. W. Brodland. Tensile properties of embryonic epithelia measured using a novel instrument. *Journal of Biomechanics*, 38:2087–2094, 2005. 2
- [55] A. Yilmaz, O. Javed, and M. Shah. Object tracking: A survey. *ACM Computing Surveys*, 38(4 2006):13, 2006. 9, 11, 12, 13